Integrated Shipboard Measurements of the Marine Boundary Layer

C. W. FAIRALL AND A. B. WHITE

NOAA/Environmental Technology Laboratory, Boulder, Colorado

J. B. EDSON AND J. E. HARE

Woods Hole Oceanographic Institution, Woods Hole, Massachusetts

(Manuscript received 3 July 1995, in final form 23 April 1996)

ABSTRACT

The NOAA Environmental Technology Laboratory air–sea interaction group and collaborators at the Woods Hole Oceanographic Institution have developed a seagoing measurement system suitable for mounting aboard ships. During its development, it was deployed on three different ships and recently completed three cruises in the Tropical Ocean Global Atmosphere Coupled Ocean–Atmosphere Response Experiment as well as two cruises off the west coast of the United States. The system includes tower-mounted micrometeorological sensors for direct covariance flux measurements and a variety of remote sensors for profiling winds, temperature, moisture, and turbulence. A sonic anemometer/thermometer and a fast-response infrared hygrometer are used for turbulent fluxes. Winds are obtained from a stabilized Doppler radar (wind profiler) and a Doppler sodar. Returned power and Doppler width from these systems are used to deduce profiles of small-scale turbulence. A lidar ceilometer and a microwave radiometer are used to obtain cloud properties. Radiative fluxes are measured with standard pyranometers and pyrgeometers. A conventional rawinsonde system gives intermittent reference soundings. The system is used to study surface fluxes, boundary layer dynamics, cloud–radiative interactions, and entrainment. It has also proven useful in satellite calibration/validations. Following a description of the systems and methods, various examples of data and results are given from recent deployments in the North Atlantic, off the United States west coast, and in the equatorial Pacific Ocean.

1. Introduction

Air–sea interaction can be considered as interactive processes between nearly geostrophic, essentially nonturbulent oceanic and atmospheric flows. The physics of the atmospheric and oceanic boundary layers plays a major role in the interaction process. The structure of the atmospheric boundary layer (ABL) is traditionally broken down into sublayers. The molecular sublayer or surface microlayer is the region a few millimeters in thickness in direct contact with the interface where turbulent processes are damped by viscosity, and vertical transport is dominated by molecular diffusion. The surface layer is the 10% of the boundary layer nearest the interface, where the height dependence of the turbulent fluxes is small and the dynamical properties are well described by Monin–Obukhov similarity (MOS) theory. The mixed layer is roughly 80% of the boundary layer where turbulent mixing has made the vertical gradients of mean properties quite small. The inversion layer is the interface between the turbulent boundary layer and the essentially nonturbulent fluid beyond; a typical thickness is about 10% of the depth of the entire boundary layer. (Details can be found in modern reference books such as Panofsky and Dutton 1984; Garratt 1992; Kraus and Businger 1994).

Within the surface microlayer, profiles and transports are naturally scaled with the kinematic viscosity ν and the diffusivities $\kappa_x = D_x/\rho$, where D_x is the diffusion coefficient for the variable x, and ρ is the density of air or water (Liu et al. 1979; Brutsaert 1982; Kraus and Businger 1994). The details are more complicated than presented here; for example, there are differences between aerodynamically rough and smooth flow, so the reader is urged to consult a rigorous treatment (e.g., Kraus and Businger 1994). This approach has been used to describe the so-called cool skin at the sea surface that results from sensible, latent, and net longwave heat transfer at the interface (Saunders 1967; Hasse 1971; Paulson and Simpson 1981; Wick et al. 1996). MOS theory is one of the most successful scaling theories in meteorology. It is based on the idea that the mean and turbulent properties of the dynamical variables can be scaled by combinations of the surface fluxes, and their height dependence can be described by the ratio of the height above the surface to the Monin–Obukhov length L (see section 2b). MOS has been applied extensively

Corresponding author address: Dr. C. W. Fairall, NOAA/ERL/ETL, R/E/ET7, 325 Broadway, Boulder, CO 80303.
E-mail: cwf@etl.noaa.gov

over the ocean and forms the basis of several surface flux estimation methods. Considerable effort has been expended in demonstrating that the over-land and over-ocean scaling properties are the same.

Land and marine ABLs have been the subject of a massive research effort involving numerous field programs and the development of numerical models of varying sophistication. The dynamics of the bulk of the boundary layer are too complex to represent by simple, general scaling models, although many properties of the convectively driven mixed layer are well represented by convective scaling (Kaimal et al. 1976). Compared to the ocean, the atmospheric boundary layer has been extensively investigated and, in many ways, is considered to be better understood. This understanding has developed from a combination of sources, 1) laboratory models (e.g., Willis and Deardorff 1974), 2) three-dimensional primitive equation large-eddy simulations, usually called LES (e.g., Deardorff 1974; Moeng 1984), and 3) atmospheric measurements with aircraft and tethered balloons (e.g., Lenschow 1973; Kaimal et al. 1976; Brost et al. 1982; Nichols 1984). Surface-based remote sensors (e.g., Lenschow 1986; Albrecht et al. 1990) are just beginning to be applied to these problems. In a review of ABL turbulence, Fairall (1987) identified seven different classes of structure and pronounced only the cloud-free convective ABL to be reasonably well understood.

Between the turbulent boundary layer and the non-turbulent free fluid is a transition region characterized by strong gradients or jumps in the dynamical variables and concentrations of various constituents. Entrainment is the process whereby this boundary is eroded by the turbulent diffusive processes of the boundary layer. The erosion process creates a vertical flux in the inversion region referred to as the entrainment flux F_i. Note that the buoyancy flux is usually negative in the inversion because the entrainment process works against potential energy and therefore destroys turbulent kinetic energy (TKE). The entrainment flux is characterized by the entrainment velocity W_e, which describes the rate of increase of ABL depth caused by turbulent mixing across the interface. Parameterizations for W_e are a key component of mixed-layer models. Such parameterizations are generally based on arguments about the sources of TKE in the mixed layer and the transport of that TKE to the inversion region (Stage and Businger 1981; Moeng et al. 1992).

Boundary-layer clouds have received increased research emphasis in recent years. The First ISSCP (International Satellite Cloud Climatology Project) Regional Experiment (FIRE) and the Atmospheric Radiation Measurement (ARM) programs are notable major efforts with ABL cloud components. Browning (1994) has identified ABL clouds as a priority issue in the parameterization of cloud-related processes in general circulation models (GCMs). Information is needed about the relationship between cloud liquid water content, fraction, geometry, and optical properties. There are also related interests: cloud condensation nuclei concentrations, cloud microphysics, drizzle production, and ABL/cloud dynamics such as decoupling of layers within the boundary layer.

Research on marine ABL dynamics and structure and cloud-radiative processes has long been hampered by a lack of suitable observing systems for the oceans. Satellite observing systems obviously offer a powerful source of ABL information over the oceans (Gautier et al. 1980; Liu 1990; Katsaros 1990), but there still exists a need for a highly capable surface-based platform for open-ocean field campaigns and near-surface research problems. A very comprehensive system is required because ABL dynamics is so complicated (i.e., it would make no sense to attempt to investigate the entrainment rate without measurements of surface fluxes, cloud properties, and ABL mean structure). In response to this need, the Environmental Technology Laboratory (ETL) air–sea interaction group has developed a ship-mountable system for measuring near-surface and ABL processes to support several ongoing research programs in marine meteorology and climate. The system presently consists of seven components assembled from a combination of commercial and in-house sensors:

1) bulk meteorological variables and radiative fluxes;
2) direct air–sea turbulent fluxes;
3) a lidar ceilometer for cloud-base height and aerosol profiles;
4) a 915-MHz radar with RASS (radio acoustic sounding system) for wind, temperature, and turbulence profiling;
5) a two-channel microwave radiometer for integrated water vapor and cloud liquid water content;
6) an Omega–Navaid-based rawinsonde system; and
7) a Doppler acoustic minisodar for high-resolution near-surface wind and turbulence profiling.

Lists of the specific instruments and their measurement capabilities are given in Tables 1 and 2.

The flux/meteorological system is the latest version of a system originally deployed in the Humidity Exchange over the Sea (HEXOS) experiment in 1987 on a North Sea platform (Fairall et al. 1990). An updated version of the system was used for the Tropical Ocean Global Atmosphere (TOGA) pilot cruise on the R/V *Wecoma* in 1990 (Young et al. 1992). The wind profiler, ceilometer, and rawinsonde system were first deployed in the Tropical Instability Wave Experiment (TIWE) cruise aboard the R/V *Moana Wave* in 1991 (Chertock et al. 1993). The microwave radiometer was added for the Atlantic Stratocumulus Transition Experiment (ASTEX) cruise aboard the R/V *Malcom Baldridge* in the North Atlantic in 1992 (White et al. 1995). All systems were again used for three, 1-month cruises (see Fig. 1) in the TOGA Coupled Ocean–Atmosphere Response Experiment (COARE) in 1992 and 1993 (Young et al. 1995; Fairall et al. 1996). The bulk meteorology/flux system has recently been deployed separately aboard

TABLE 1. List of shipboard in situ and near-surface instruments used by ETL.

System No.	Instrument	Type	Measurement
1	Thermometer	Vaisala HMP-35	Air temperature
1	Hygrometer	Vaisala HMP-35	Mean humidity
1	Thermistor	YSI 46040	Sea surface temperature
1	Pyranometer	Eppley PSP	Solar irradiance
1	Pyrgeometer	Eppley PIR	Downward IR irradiance
1	Optical rain gauge	STI ORG-100	Precipitation
2	Sonic Anemometer	Gill Solent	Wind vector, stress, and heat flux
2	IR hygrometer	OPHIR IR2000	Moisture flux
2	GPS	Navastar XR4-PC	Course and speed
2	Gyrocompass	Robertson RGC-10	Heading
2	Strapdown navigation	ETL	Mast motions
2	Inertial navigation	Pandect VRG-105	Ship motions

the *Floating Instrument Platform* (R/P *FLIP*) and the remote sensing system aboard the R/V *Titan* in the San Clemente Ocean Probing Experiment (SCOPE) in 1993 (Fairall and Edson 1994); the flux system was deployed by itself aboard the R/V *Glorita* in the Ship Tracks experiment off California in 1994. Finally, the complete system (including the recently added minisodar) was deployed in the marine boundary layers (MBL) experiment off Monterey, California, in April and May 1995.

In this paper the authors describe the system and its capabilities, and show how it has been used. Discussion of individual components will be limited primarily to issues specific to implementation on ships. Rather, the focus will be on how the components are linked together to form a system and the technology and techniques used to derive useful information. Sections 2 and 3 of the paper discuss turbulent flux methods and the specific implementation used (sensors, data processing, etc.). In section 4 the various remote sensors are discussed. Sample applications from recent cruises are discussed in section 5. Conclusions and immediate plans are given in section 6.

2. Methods of measuring near-surface turbulent fluxes

a. Background

The conservation equation for the ensemble mean of variable x, denoted as X, is

$$\frac{\partial X}{\partial t} + \nabla_h X \cdot \mathbf{u}_h = -\frac{\partial(\overline{w'x'})}{\partial z} + \bar{Q}_x, \qquad (1)$$

where the subscript h denotes horizontal components and Q_x represents the source term. The quantity of interest is the Reynolds flux enclosed in the parentheses. The flux can be determined by measuring the time or space series of w' and x' and computing their mean cross product; this is referred to as the covariance or eddy-correlation method. Alternatively, the other terms in (1) could be measured and the vertical gradient in the flux computed as a residual; this is referred to as the budget method.

In this paper the authors will focus on methods that are based on point measurements at a fixed location within the ABL. Besides the covariance method, there is a host of other more indirect, local-method approaches based on applications of MOS to measured properties other than the covariances. Note that these other methods yield estimates of the surface flux only, while the covariance method is general. This diversity of methods for measuring fluxes is primarily due to the historical difficulty, expense, and impracticality of making the direct covariance measurements for all variables of interest on the horizontal and temporal scales of interest. Measurements over the ocean involve the additional complication of platform motion (Fujitani 1985), flow distortion by booms, other instruments, and the platform (Oost et al. 1994), and contamination by sea spray and salt particles (Schmitt et al. 1978). Fast-response sensors are still not available at this writing for a number of gas and particle species of interest. More complete information on flux methods can be found in Businger (1986), Donelan (1990), Geernaert (1990), and Kraus and Businger (1994). Details on the specific inertial-dissipation and bulk-flux algorithms used for this work are given in Fairall et al. (1996).

TABLE 2. Profiling sensors used for shipboard operation by ETL.

System No.	System	Type	Measurement
3	Ceilometer	Vaisala CT-12K	Aerosol scat., cloud-base height
4	Wind profiler	915 MHz ETL/AL	Wind and turbulence profiles
4	RASS	915 MHz/1.9 kHz	Boundary layer temperature
5	Microwave radiometer	Radiometrics WVR-1000	Water vapor and liquid
6	Rawinsonde	NCAR class	Wind, temperature, and humidity
7	Minisodar	Aerovironment	Wind and turbulence profiles

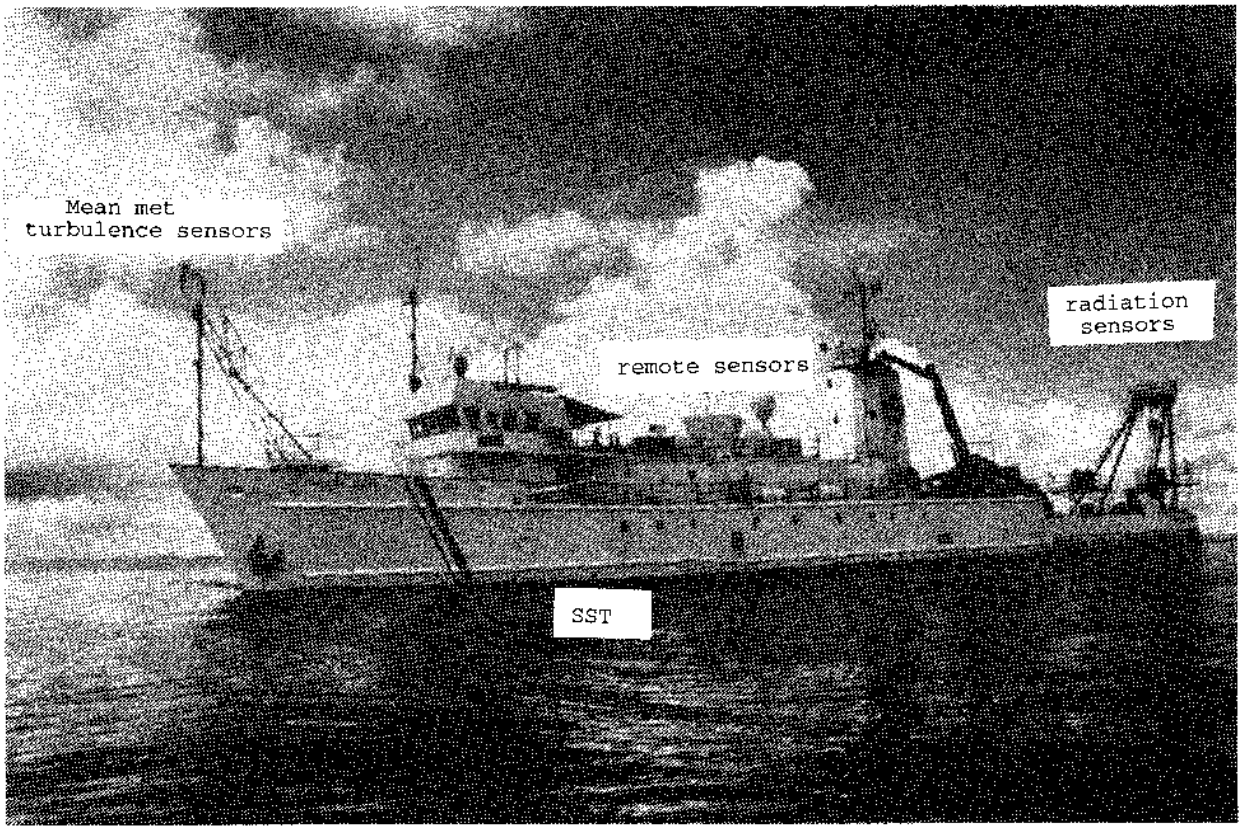

FIG. 1. Photograph of the R/V *Moana Wave* with the ETL system during COARE.

b. Turbulent flux methods

1) COVARIANCE METHODS

As discussed above, the eddy correlation is the standard upon which the other local methods are based. In principle, once sensor calibration errors and other sources of error (e.g., flow distortion, contamination, or platform motion) are removed and the sensors have adequate frequency response to resolve the relevant scales of turbulence (about 10 Hz), covariance computations represent an unbiased estimate of the true ensemble mean of interest at the height of the measurement [see Businger (1986) or Donelan (1990) for a discussion of the difference between the flux at height z and the true surface flux]. From a practical point of view, we do not measure the actual ensemble average, but compute estimates from time–space series of data taken on towers, platforms, ships, aircraft, etc. Traditionally, strict requirements for covariance measurements are not enforced, but a particular measurement (say a 1-h average) is considered to be an estimate of the true flux subject to some statistical sampling uncertainty (Wyngaard 1973; Fairall 1984; Lenschow and Kristensen 1985). For 1-h averages, this uncertainty is on the order of 20%, but is highly dependent on conditions. It is assumed that the effects of the random sampling error can be reduced by averaging a collection of flux values. The choice of averaging period is not arbitrary; Mahrt et al. (1996) discuss trade-offs between high-pass filtering the time series, the timescale of the average computation, and nonstationarity of the data. High-pass filtering and tapering are done to combat the unwanted effects of nonstationarity and/or spectral leakage (Kaimal et al. 1989). A variety of techniques is used including block averages, running mean filters, and no filtering at all, but rejecting samples where the cospectra are not well behaved at low frequency (see Oncley 1989, for a discussion of the ogive).

Alternatives to the covariance method were originally developed due to a lack of fast-response sensors, a condition existing today for many chemical species. An interesting variation of the covariance method, referred to as the relaxed eddy accumulation (REA) method, has been developed (Businger and Oncley 1990; Pattey et al. 1993). The method is usable if a sensor is available that can accurately measure differences in concentration of the constituent. However, the method does not rely on MOS or empirical stability functions.

2) MOS METHODS

In the surface layer, scaling parameters are defined in terms of the turbulent fluxes:

$$x_* = -\frac{(\overline{w'x'})_o}{u_*}, \tag{2}$$

where $x = u$, T, or q (i.e., velocity, temperature, or humidity), and the zero subscript denotes the surface value of the flux. MOS is based on the idea that in the surface layer the dynamical variables can be scaled by combinations of these parameters plus the height, z, and that the dimensionless properties are then functions of $\xi = z/L$, where L is the MOS scaling length, and

$$\xi = \frac{\kappa g z}{T}\frac{(T_* + 0.61Tq_*)}{u_*^2}, \tag{3}$$

where g is the acceleration of gravity and κ is the von Kármán constant. Garratt (1992) lists values of κ from nine field programs conducted in the 1970s and 1980s and suggests $\kappa = 0.4$.

Details on MOS can be found in the texts referenced above, but a few examples are given here. The vertical gradient of the mean of some variable X can be represented by

$$\frac{\partial X}{\partial z} = \frac{x_*}{\kappa z}\phi_x(\xi), \tag{4}$$

where ϕ_x is an empirically determined dimensionless gradient function. We can integrate (2) to describe the profile (Paulson 1970)

$$X(z) - X_o = \frac{x_*}{\kappa}\left[\ln\left(\frac{z}{z_{ox}}\right) - \Psi_x(\xi)\right], \tag{5}$$

where z_{ox} is the surface roughness length and Ψ_x the dimensionless profile functions. Similarly, we can represent the dissipation rate by

$$\epsilon = \frac{u_*^3}{\kappa z}\phi_\epsilon(\xi) \tag{6}$$

and the structure function parameter for the variable x by (Wyngaard et al. 1971)

$$C_x^2 = x_*^2 z^{-2/3} f_x(\xi). \tag{7}$$

Again, ϕ and f are dimensionless MOS similarity functions. The forms of the MOS functions must be determined by measurements, but their asymptotic behavior for the stability extremes (convective, $\xi \to -\infty$; stratified, $\xi \to +\infty$) are predicted by the theory of Wyngaard (1973).

The primary MOS-based flux estimation methods in use are the gradient/profile, the bulk, and the inertial-dissipation methods. As stated before, these methods rely on dimensionless functions that must be determined empirically using covariance measurements as the standard. Most of the relevant functions have been first measured over land and then either assumed or verified to be applicable over the ocean. The gradient method with the ship system is not being used here, so it will not be discussed further.

The inertial-dissipation method is based on MOS forms for the high-frequency portion of the variance spectra. This method has been used extensively to measure drag coefficients over the open ocean (Large and Pond 1981, 1982). The method was reviewed by Fairall and Larsen (1986) and analyzed in detail by Edson et al. (1991). Besides ships, the method has been used on aircraft (Fairall and Markson 1987) and buoys (Skupniewicz and Davidson 1991). Papers describing ship implementations of this method are still appearing in the literature (Fairall et al. 1990; Yelland et al. 1994).

The main attraction of the inertial-dissipation method is its use of the high-frequency portion of the spectrum where platform motions are overwhelmed by turbulence signal. The commercial development of reliable sonic anemometer/thermometers and infrared hygrometers has provided the required frequency response. There is a minor distinction between using actual measurements of dissipation rates by integrating over the derivative spectrum (8a) versus using a fit to the Kolmogorov $-5/3$ power law in the inertial subrange (8b) to determine the appropriate structure function parameter (see discussion in Fairall et al. 1990). For example,

$$\epsilon = \frac{15\nu}{U^2}\int \omega^2 S_u(\omega)\, d\omega, \tag{8a}$$

$$C_u^2 = 4U^{-2/3}\omega^{5/3}S_u(\omega), \tag{8b}$$

where, in this case, S_u is the streamwise velocity spectrum as a function of angular frequency ω.

Direct dissipation methods are rarely used over the ocean because sensors do not exist that can measure temperature and humidity fluctuations to 5 kHz in the ocean environment, and the velocity sensors (hot wires) require frequent replacement. Thus, comments here will be restricted to the inertial subrange method, which requires frequency response on the order of 10–100 Hz. Following determination of the structure functions via (8b), there are two basic approaches used. The structure functions themselves are used directly with (7), and the fluxes are found by iteration. Alternatively, the structure functions may be converted to dissipation rates via the Corrsin relations:

$$\epsilon_x = \frac{C_x^2\epsilon^{1/3}}{4\beta_x}, \tag{9}$$

where ϵ_x is the relevant dissipation rate, $\beta_u = 0.54$ and $\beta_T = \beta_q \approx 0.80$. In this second approach, the dimensionless MOS function comes from empirical determinations of the TKE and scalar budget balances as a function of stability. Typically,

$$\phi_\epsilon(\xi) = \phi_u(\xi) - \xi, \tag{10a}$$

$$\phi_{\epsilon T} = \phi_T(\xi). \tag{10b}$$

To the extent that the Kolmogorov constants are known, these two approaches are exactly equivalent. The $f_x(\xi)$ functions are related to the dimensionless dissipation

functions via (9). However, the forms of $f_x(\xi)$ that best fit the structure function data are not guaranteed to yield (10). Recent work (Vogel and Frenzen 1992; Fairall and Edson 1994) indicates that (10) is not exactly correct and that some small adjustments are required to further improve the mean accuracy of the method.

The inertial-dissipation method works best with velocity; excellent correlations of covariance or bulk stress are routinely obtained with this method. Today's sonic temperature signals are free from salt contamination but have rather high noise levels (Larsen et al. 1993), so inertial-dissipation sensitivity for sensible heat flux is not as good as other methods for typical open-ocean conditions. There is also extreme sensitivity to contamination by ship heat island effects. Modern commercial fast hygrometers have adequate sensitivity but are still subject to a variety of problems (salt contamination, radio frequency interference) that can produce particularly unsatisfactory effects in the variance spectrum.

The bulk method has a long history of application. It plays a special role because it can be used to estimate fluxes from historical datasets and because it is essential in establishing the lower boundary condition in numerical models. The accuracy of the method has been discussed extensively by Blanc (1985, 1986, 1987). The standard bulk expressions for fluxes are given by

$$\overline{w'x'} = \frac{c_{dn}^{1/2} c_{xn}^{1/2} S(X_s - X_r)}{\left[1 - \frac{c_{dn}^{1/2}}{\kappa}\Psi_u(\xi)\right]\left[1 - \frac{c_{xn}^{1/2}}{\kappa}\Psi_x(\xi)\right]} = C_x S(X_s - X_R), \tag{11}$$

where c_{dn}, c_{Tn}, and c_{qn} are the transfer coefficients for velocity, temperature, and moisture; the subscript n refers to the neutral value ($\xi = 0$), and the transfer coefficients for stress and sensible and latent heat are denoted by C_x. Here X_s is the mean variable value at the surface, and X_r the value at some reference height z_r. Note that in this convention $X = U_1$, U_2 are the horizontal wind components relative to the fixed earth, and S is the average value of the wind speed relative to the sea surface at z_r. Measurements of winds, temperature, humidity, and sea surface temperature are used with (11); the solution is found iteratively.

The neutral transfer coefficients are related to the roughness lengths, which are defined as the height where the extrapolation of the log$z$ portion of the variable profile intersects the surface value

$$c_{xn}^{1/2} = \frac{\kappa}{\ln(z_r/z_{ox})}. \tag{12}$$

The velocity roughness length z_o is often crudely related to the physical roughness of the surface (see Panofsky and Dutton 1984, 123), but the scalar roughness lengths are more complicated. This is discussed in detail in chapters 4 and 5 of Garratt (1992) or chapter 5 of Kraus and Businger (1994). Smith (1988) has expressed the roughness length as the sum of a smooth flow limit and a Charnock (1955)–type dependence:

$$z_o = \frac{\alpha u_*^2}{g} + \frac{0.11\nu}{u_*}, \tag{13}$$

where α is the Charnock ''constant'' for which values between 0.010 and 0.035 can be found in the literature (e.g., Garratt 1992, Table 4.1). The value of the Charnock constant can be linked to gross characterizations of the sea state (Geernaert 1990), such as the age or slope of the dominant wavelength (from the peak of the gravity wave spectrum).

Another topic of interest is the form of the transfer coefficients in the limit of low wind speed. Note that in (11) the parameter S is in fact the average value of the wind speed, not the magnitude of the mean wind vector. Godfrey and Beljaars (1991) have expressed S as

$$S^2 = u_x^2 + u_y^2 + w_g^2 = u^2 + w_g^2, \tag{14}$$

where u_x and u_y are the mean wind components, and w_g is proportional to the convective scaling velocity as follows:

$$w_g = \beta W_*, \tag{15}$$

where β is an empirical constant of the order unity, and β depends on the temporal/spatial scale used to compute the averages.

3. Near-surface flux/meteorological system implementation

The heart of the turbulent flux system consists of a sonic anemometer/thermometer and an infrared fast hygrometer. Both instruments have been specifically selected for their ability to withstand the harsh marine environment and deliver usable data despite nominal contamination with water and salt. The remainder of the meteorological instruments are high-quality commercial units. Fluxes are computed in real time using three methods: (a) eddy covariance, (b) inertial dissipation, and (c) bulk aerodynamic algorithms (as described in section 2). A ship motion measuring system (Hare et al. 1992) is used to provide data to correct the sonic anemometer wind data to eliminate ship and boom motion contamination that invalidates most seagoing eddy covariance stress measurements. The scalar fluxes are much less affected. The system consists of a gyrostabilized triaxial accelerometer set mounted near the ship's center of motion and a ''strapdown'' triaxial accelerometer set and triaxial angular rate unit mounted on the mast as an integral part of the sonic anemometer base. Ship's course and speed are obtained from a Global Positioning System (GPS) receiver, ship's heading from a gyrocompass. The flux and bulk meteorological sensors are placed on a mast near the ship's bow (see Figs. 1 and 2). Mean flow tilt angles at this location are typically around 5°, which were considered to be within an acceptable range for ship-induced flow distortion effects on the fluxes

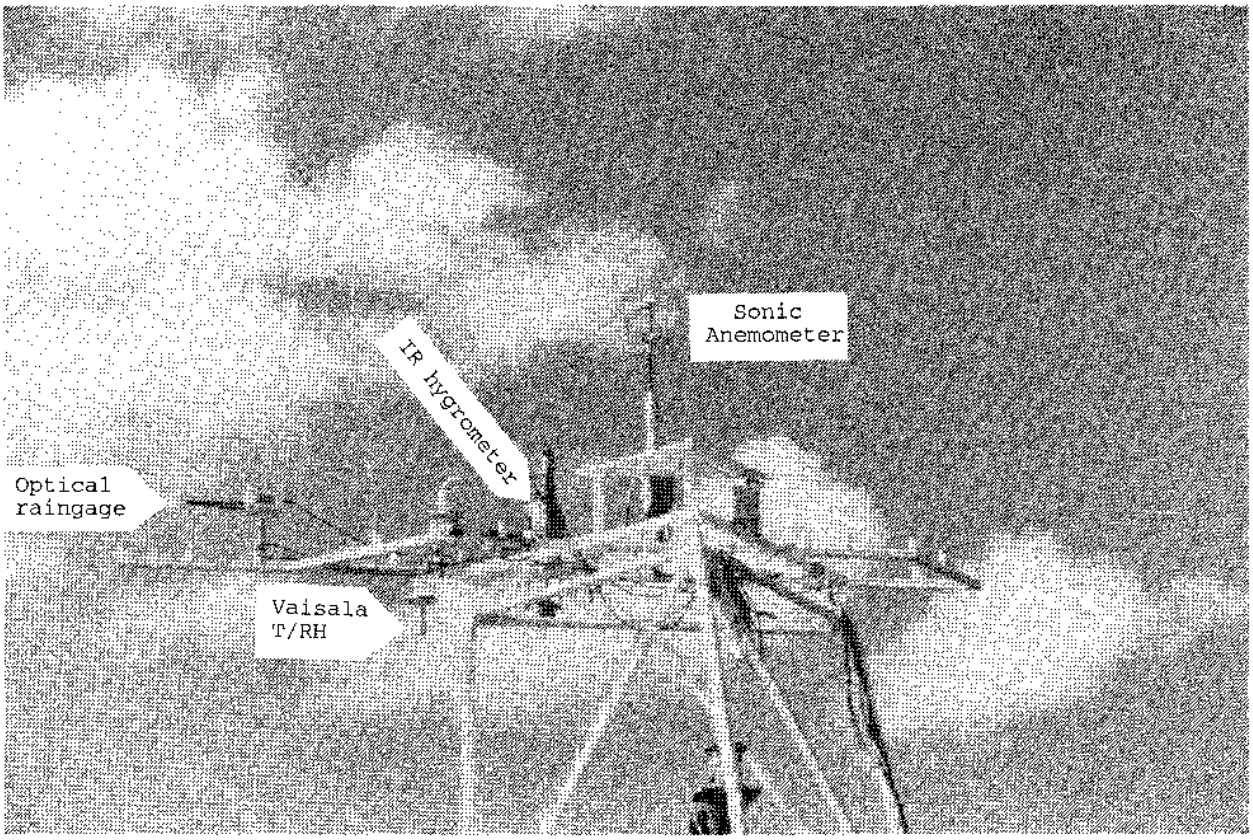

FIG. 2. As in Fig. 1 but a close-up of sensors on the bow mast.

(Edson et al. 1991; Oost et al. 1994). For a continuous operation mode, this location was preferable to a bow spar, which usually cannot be left deployed in rough weather, and a ship's mast just aft of the pilot house, which has numerous sources of electromagnetic interference and close contact with stack gases. The radiative flux sensors are usually not mounted on the bow mast, but at some other well-exposed location on the ship.

a. Motion corrections

The techniques used to correct turbulence data for ship motion will be briefly sketched here; details can be found in J. Edson et al. (1997, manuscript submitted to *J. Atmos. Oceanic Technol.*).

1) BASIC EQUATIONS

A variety of approaches have been used to correct wind sensors for platform motion. True inertial navigation systems (Axford 1968; Lenschow and Spyers-Duran 1987) are standard for research aircraft. These systems are expensive and subject to the so-called Schuler oscillation, so simpler techniques have been sought for ships (where the platform mean vertical velocity is unambiguously zero). The basic approach we are using follows that of Fujitani (1985). The true wind vector (i.e, uncontaminated by motion) can be written as

$$\mathbf{u} = \mathbf{T}\mathbf{u}_t + \mathbf{V}_{cg} + \boldsymbol{\Omega} \times \mathbf{T}\mathbf{M}, \tag{16}$$

where $\mathbf{u}_t$ is the wind speed measured by the anemometer in the ship (or anemometer) reference frame that is rotated relative to an earth-fixed (north, west, and vertical) frame, $\mathbf{T}$ is a matrix that rotates vectors in the ship frame back to the fixed frame, $\mathbf{V}_{cg}$ is the translational vector of the ship's center of gravity, $\boldsymbol{\Omega}$ is a vector describing the angular velocity of the ship in the fixed frame (i.e., rotation rates about the *N, W,* and *Z* axes), and $\mathbf{M}$ is a spatial displacement vector from the ship's center of gravity to the anemometer.

Note that if the motion-measurement system is not located at the center of gravity, but at some location $\mathbf{S}$, then the direct integrations of the accelerations must be corrected for angular motions (Fujitani 1985) and the vector $\mathbf{M}$ in (16) is replaced by the $\mathbf{R} = \mathbf{M} - \mathbf{S}$, which is the vector representing the separation of the motion unit and the sonic anemometer.

2) ETL APPROACH

For the purpose of redundancy and in investigating different approaches, the authors have used a mechan-

ical gyrostabilized system located near the ship's center of gravity and a strapdown system mounted on the mast with the sonic anemometer. The mechanical system has electronic pick-offs to deliver conventional pitch and roll and three accelerometers mounted in the stabilized platform. Thus, accelerations are measured in a vertically fixed frame. The term strapdown refers to the fact that all sensors measure in the ship frame (i.e., it is strapped down to the ship). The mast sensor contains three accelerometers and three angular rate sensors in triaxial mounts. These units are permanently fixed to a precisely machined flat on the side of a vertically oriented aluminum cylinder. The sonic anemometer bolts directly to the top of the cylinder. Thus, the relative orientation of the sonic anemometer and the mast motion unit are fixed and known. While the ship is in port, the mast is adjusted until the horizontal accelerometers read near zero. This is done to an accuracy of a few tenths of degrees. The gyrostabilized unit in the laboratory is shimmed at its floor mounts until the pitch-and-roll angles read zero. The horizontal accelerations normally read zero because of the gravity erection. The gyrocompass mount is adjusted so the indicated heading agrees with the ship's gyrocompass, and the mast unit yaw orientation is adjusted using as heading reference a magnetic compass that temporarily mounts in the anemometer position. As noted in Table 1, the gyrostabilized unit is a Pandect vertical reference gyro, model 105. It uses Sunstrand Data Control Inc. mini-pal accelerometers. The mast unit uses Sunstrand QA-2000-020 accelerometers and Systron Donner QRS11-100 quartz angular rate sensors. Systron Donner now offers a combined accelerometer and angular rate measurement sensor in a small convenient package under the model name MotionPak.

Our initial investigations gave better results using the mast-mounted unit for accelerations, so we will restrict our further discussion to that approach. When mounted on a ship, the $\mathbf{\Omega}$ term is negligible for the mast unit because $\mathbf{R}$ is less than 1 m. Note that either unit may still be used to determine the angles and the capability to switch between the units in case of failure of one sensor has been maintained.

3) MOTION PROCESSING

The ship-frame angular rates are first high-pass filtered, then integrated and high-pass filtered again. The mean tilt of the ship may be ignored or referenced to the mean angles from the pitch-and-roll gyro; the mean heading must be referenced to the gyrocompass. At present, the integrated yaw rate is not used, only the direct readings of the gyrocompass. The mean tilts may also be referenced to the horizontal accelerations using complementary filtering (Hare et al. 1992). A time constant of 5 min for the angular rates and 2 min for the angles is being used.

To illustrate the actual processing of the velocity data, (16) is rewritten as

$$\mathbf{u} = \mathbf{T}\mathbf{u}_t + \mathbf{V}_{\rm lp} + \mathbf{V}_{\rm hp} + \mathbf{\Omega} \times \mathbf{T}\mathbf{R}, \qquad (17)$$

where the ship velocities have been divided into low-pass (lp) and high-pass (hp) components. The high-pass components are computed by integrating accelerations in the fixed frame (minus gravity in the vertical coordinate) and high-pass filtering the resultant velocities:

$$\mathbf{V}_{\rm hp} = \mathrm{Hp}\left[\int (\mathbf{T}\mathbf{a}_t - g\mathbf{i}_z)\, dt\right], \qquad (18)$$

where Hp represents a high-pass filter operator, $\mathbf{a}_t$ the strapdown accelerations, g the acceleration of gravity, and $\mathbf{i}_z$ the unit vector in the vertical direction. This component represents the wave-induced motions of the anemometer, typically using a time constant of 2 min for the high-pass filter. The low-pass component is computed only for the horizontal velocities; either GPS, the ship's acoustic Doppler current profiler (ADCP) upper-range gates, or the ship's Doppler speed log can be used. The latter two reference the wind speed to the water, while the GPS approach references to the fixed earth. Because for most air–sea interaction applications the air–water velocity difference is more relevant, GPS-referenced winds should be corrected with measurements of surface current (if available). For real-time processing we use simple exponential time filters and compute fluxes in 10-min blocks. The low-pass term is applied as a mean correction at the end of the averaging period (i.e., the low-pass time constant is 10 min). For postprocessing we use time-symmetric filters and apply the smoothed GPS data at every time step. Either way, stress values tend to be invalidated by ship maneuvers. Thus, underway at a constant heading or drifting are the preferred modes for good flux data.

b. Data acquisition

Two computers are used to acquire and process the data: a 486 PC for all motion measurements and computations and an HP382 workstation for meteorological measurements and final application of (17) in real time. The PC acquires the gyrocompass on RS-232; the GPS data is a card installed in the computer bus. An analog-to-digital (A/D) converter card is used to acquire the mast unit (three accelerations, three angular rates, and unit temperature) and the gyro (three accelerations, pitch, and roll) signals. The analog signals are antialias filtered and digitized at 5 Hz; significant vibration noise has been found on the accelerometers (particularly on the mast) in the 5–10-Hz range when the ship is underway at full power. The filtering, rotations, and integrations described above are computed in real time on the PC and raw and processed motion information (20 channels at 5 Hz) is passed to the HP computer via RS-232.

In addition to the motion information, the HP acquires the sonic anemometer and the hygrometer on RS-232 and runs a slow data acquisition system that digitizes about 10 channels of data (mean air and water temperature, humidity, radiative fluxes, rain rate, and any other variables of specific interest). The HP system has been described previously (Fairall et al. 1990) so only a few details will be mentioned here. Data is acquired in dual-buffered, 12.8-s blocks, and computations are done in quasi-real time (i.e., on 12.8-s delay). The anemometer and fast hygrometer are preaveraged and/or interpolated to 10 Hz. Following motion corrections, accumulations are done for mean, variance, and covariances; spectra are computed for the 12.8-s blocks and accumulated. A Hamming time-taper window is used for spectral computations (Edson et al. 1991). At the end of 10 min, means and variances are computed for slow and fast variables, covariances and mean spectra are computed for fast variables, and the raw time series (10 Hz for turbulence, 5 Hz for motion, and 1/12.8 Hz for slow variables) is stored. Covariances in streamwise coordinates are computed by standard rotation into the mean flow (Tanner and Thurtell 1969). Raw covariances, coordinate-rotated covariances, and ship-motion-corrected plus coordinate-rotated covariances are all computed and compared. Raw and motion-corrected variance spectra are also computed. The 10-min average data are stored and accumulated and a grand average computed and stored every 50 min. At present, cospectra are only computed in postprocessing.

c. *Turbulence sensors*

1) SONIC ANEMOMETER

Signals from a sonic anemometer/thermometer and an infrared hygrometer are combined for computation of three principal turbulent fluxes. To avoid salt contamination effects (Schmitt et al. 1978), sonic temperature is used to derive sensible heat flux. Corrections are required for the influence of humidity and there are two forms of velocity contamination (Schotanus et al. 1983; Larsen et al. 1993). Sonic anemometers use the times of flight of acoustic pulses in alternating directions between pairs of transducers. The difference in the inverse time gives the wind component and the mean of the inverse time gives the speed of sound (used to derive air temperature). One form of velocity cross talk is caused by the time delay between pulses in different directions; this does not affect the w–T covariance, but contaminates the temperature variance spectrum (Larsen et al. 1993). The other form of cross talk is caused by lengthening of the sound path by the wind speed normal to the path S_n used to compute the sonic temperature (Schotanus et al. 1983; Mortensen 1994):

$$T_{sn} = \frac{l^2}{4\gamma_d R_d}\left(\frac{1}{t_1} + \frac{1}{t_2}\right)^2 + \frac{S_n^2}{\gamma_d R_d}, \qquad (19)$$

where l is the acoustic path length, t_1 and t_2 the travel times in each direction, γ_d the ratio of pressure and volume specific heats, and R_d the gas constant for dry air. For a vertically oriented temperature path, $S_n^2 = U_1^2 + U_2^2$ (i.e., the horizontal wind speed squared). We have used the Applied Technologies Incorporated (ATI) sonic model SWS-211/3K on the COARE pilot and the TIWE cruises. This unit has a vertically oriented temperature channel, but it performs this correction in internal software and delivers corrected sonic temperature. On subsequent cruises we used the Gill Solent anemometer, which has a trisymmetric configuration, and the temperature channel is from the S_1 transducer pair. For this sonic $S_n^2 = U_2^2 + 0.5(U_1 + U_3)^2$, where the U components are in the Gill coordinates. We normally mount the Gill with the U_1 axis 30° counterclockwise from the ship's bow. This correction is applied at every time step to avoid velocity contamination of the w–T correlation and the T variance spectrum.

2) IR-HYGROMETER

We have been using an OPHIR model IR-2000 for all field programs since the COARE pilot experiment. Early experiences with these devices were described by Fairall and Young (1991). The hygrometer (Cerni et al. 1987) uses a rotating filter wheel to measure light transmission at a clear channel (I_o at 2.6-μm wavelength) and an absorbed channel (I_a at 2.5 μm). The separation of the bistatic elements is 26 cm, but a mirror is used to fold the transmission path once for a total optical path of 56 cm. Raw readings of I_o and I_a are available on RS-422 at 20 Hz; adjacent pairs of points are averaged to reduce the data to 10 Hz. Water vapor density Q is computed from the ratio of the two intensities from an equation that depends on ambient pressure, temperature, and the internal temperature of the device (Fairall and Young 1991).

In clean, fair weather conditions, the hygrometer yields very high quality fast humidity data. The sensitivity is adequate for the marine conditions encountered. The hygrometer is subject to several sources of interference that may degrade its performance. When the optics become wet because of rain or sea spray, the data become unreliable (or, in an extreme case, nonexistent). There have also been problems with radio and radar interference. Because the unit is an optical device, it is also subject to errors caused by sunlight entering the optics. This may occur with a direct path or reflection from nearby shiny surfaces or a very smooth ocean. For this reason, the hygrometer is mounted with the optical entrance facing down. Horizontal mounting is more advantageous for rain cleaning of the optics, but it is our experience that ships too often orient themselves to point this instrument into the sun. Even with vertical mounting, sun interference still occurs, particularly when the ship is pitching and rolling enough to give the correct geometry for a strong reflection of sunlight

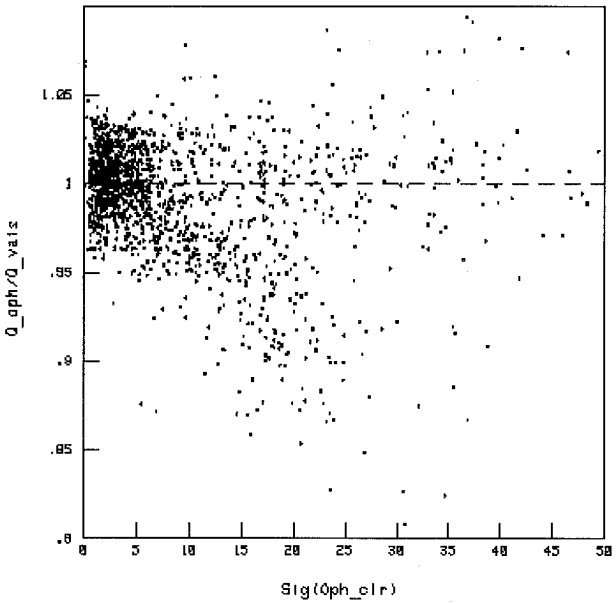

FIG. 3. The ratio of OPHIR to Vaisala HMP-35 mean humidity as a function of the standard deviation of the OPHIR clear channel counts (night only).

into the instrument resulting from either a smooth ocean surface or glint from a wave. Finally, we have observed performance deterioration with accumulation of sea salt on the optics; obviously this is a strong function of whitecapping. We have developed a simple technique for monitoring the contamination of the system by computing the standard deviation of the clear channel intensity (σ_o), which should be unaffected by fluctuations in humidity. Figure 3 shows the ratio of the mean absolute humidity output by the OPHIR normalized by an aspirated Vaisala system as a function of σ_o. These data are for nighttime only to eliminate confusion with sun interference. Note the two branches of the occurrence of the points: one branch for unaffected behavior and another for significant errors in mean humidity. There is also a strong correlation of reduction of mean humidity reading with decreasing values of the mean value of I_o. Because we do not understand the cause of the effect of salt contamination on this instrument, we cannot explain this behavior. However, we use σ_o as an indicator to clean the optics or to reject data in postprocessing. The contamination effect is much greater for inertial-dissipation fluxes, which depend directly on the variance spectrum. However, the w–Q covariance is also affected. An analysis of the same data shown in Fig. 3 indicates an average reduction in latent heat flux of 10% for $20 < \sigma_o < 40$ and 25% for $40 < \sigma_o < 100$. The σ_o test can also be used to screen data for sun, rain, and radio/radar interference.

3) SLOW SENSORS

Because of the accuracy and reliability of the sonic anemometer, we use it for mean wind speed data. This instrument is not suitable for mean temperature measurement; we use a conventional aspirated temperature–relative humidity system. We have discovered that the aspirator does not completely eliminate solar-induced radiational heating. Based on intercomparisons against a specially designed aspirated wet/dry-bulb system (E. Bradley 1993, personal communication), we are using a simple correction for solar radiation error,

$$T_{\text{air}} = T_{\text{meas}} - \frac{R_s}{700S^{1/2}}, \tag{20}$$

where R_s (W m^{-2}) is the solar flux and S (m s^{-1}) is the relative wind speed. This correction reduces light wind, afternoon temperature errors from nearly 1 K to a few tenths of a degree. The sea surface temperature (SST) is measured with a precision thermistor that is epoxied into a brass plug in the end of a sealed tygon tube. The sensor is dragged through the water from an outrigged boom about 4 m from the ship's hull. The sensor may or may not be in the ship's wake, depending on the ship and the mounting circumstances. The sensor is held near the surface by the buoyancy of the hollow tygon tube. We estimate the typical depth of the sensor to be 5 cm. We usually leave the sensor deployed while the ship is underway unless the ship speed gets over about 6 m s^{-1}, at which point it becomes more difficult to maintain steady contact with the water.

Conventional commercial pyranometers and pyrgeometers are used for measurement of solar and downwelling IR irradiances. Upward fluxes are computed from the measured SST assuming an oceanic albedo of 0.055 and a surface emissivity of 0.97 (Fairall et al. 1996). The downward IR flux is computed from direct measurements of the thermopile output and the dome and case temperatures following Albrecht and Cox (1977). We have found unreliable performance using the battery temperature compensation supplied by the manufacturer. Note that accurate IR fluxes definitely require dome temperature compensation, either by measuring the dome temperature or using the solar flux empirical correction of Alados-Arboledas et al. (1988). Solar-induced errors can easily be as large as 25 W m^{-2}. No attempt is made to gimbal or correct for angular errors from ship motion (Katsaros and DeVault 1986; MacWhorter and Weller 1991). Our own experience from intercomparing ensembles of the sensors (Ruffieux et al. 1995) suggests that factory calibrations are uncertain by 3%–5% for the pyranometer and 5–10 W m^{-2} for the pyrgeometer. For COARE special in situ intercomparisons and postcalibrations were used to reduce these uncertainties to about 2% and 2.5 W m^{-2}, respectively.

d. Sensor performance

Both types of sonic anemometer we have used deliver high-quality data and stand up to the marine environment very well. One critical test of anemometer tur-

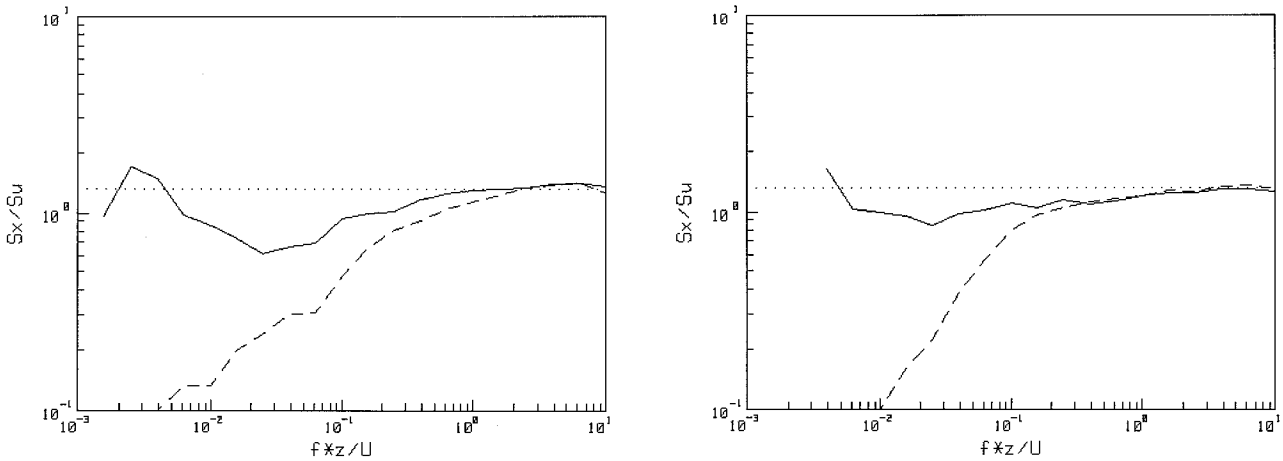

FIG. 4. Ratio of averaged velocity spectra as a function of normalized frequency. The solid line is S_v/S_u, and the dashed line is S_w/S_u: (a) $z/L = -0.2$ and (b) $z/L = -2.0$.

bulence performance is the behavior of its measured spectra in the inertial subrange. This is illustrated in Fig. 4, where the ratios of two cross-stream velocity component spectra to the streamwise spectrum are given as a function of frequency. These data are from the SCOPE experiment. Each graph represents the average of approximately 50 spectra (each one 50-min sample) at two different MOS stability classes. In the inertial subrange (high frequencies) we expect this ratio to be 4/3; as frequency decreases, we expect the vertical spectrum to decrease rapidly. At low frequencies the S_v/S_u ratio depends on ABL structure and mesoscale processes. We also expect the inertial subrange to extend to lower frequencies for the more unstable case (Kaimal et al. 1972). Notice that the more unstable case exhibits the expected behavior, and the break at the inertial subrange occurs for fz/U on the order of 3. For the more neutral case (stronger winds) there is an indication that the ratio exceeds 4/3, suggesting some small deficiencies in the anemometer's internal corrections for structural flow distortion (Mortensen 1994). Figure 5 shows spectral plots of the average streamwise and cross-stream stress cospectra (normalized by the mean streamwise covariance) for the near-neutral case. Note the well-behaved *wu* cospectrum and the negligible *wv* cospectrum, indicating that the turbulence and mean wind are well aligned. Average variance spectra for sonic temperature and humidity are shown in Fig. 6a and cospectra with vertical velocity in Fig. 6b for the near-neutral case. Note the strong similarity of these spectra. The temperature spectrum turns upward at high frequencies as the signal reaches the noise level of the sonic thermometer; there is also a tendency for the *wq* cospectrum to decrease at high frequencies because covariance is reduced by the physical separation of the anemometer and the hygrometer (Kristensen et al. 1997).

Fluxes and mean meteorological variables have been intercompared with buoys and other ships in the TIWE (Fairall and McPhaden 1993) and COARE (Fairall et al. 1996; E. Bradley et al. 1997, manuscript submitted to *J. Atmos. Oceanic Technol.*) programs. These studies form the basis for the measurement accuracies claimed in Table 3. Here only one example from these comparisons is given. Figure 7 shows latent heat fluxes measured from the R/V *Moana Wave* and the R/V *Franklin* during two periods in COARE. Covariance and bulk fluxes from both platforms are shown. The two ships are not collocated at all times during the intercomparison; collocation is indicated by the presence of covariance values for the *Franklin.* Note that on the first intercomparison a separation of some 15 km made no difference in the bulk fluxes, whereas on the second intercomparison, it did (the period from 0600 to 1800 UTC on the second day).

4. Remote sensors

The remote sensors presently in operation are listed in Table 2; several can be seen in Fig. 8. There are active systems (ceilometer and wind profiler), passive systems (microwave radiometer), and remote in situ sensors (rawinsonde). The pyranometer and pyrgeometer are also passive remote sensors. The ceilometer, pyranometer, and pyrgeometer may be considered as cloud sensors. The wind profiler was originally designed as a wind-profiling system, but returned power and spectral width data from this instrument have proven useful for cloud and ABL turbulence purposes (White and Fairall 1991; White et al. 1995, 1996). The microwave radiometer measures integrated water vapor and integrated liquid water; thus, it is both a clear-air and cloud sensor. Combining profiler, ceilometer, and radiometer data has proven very useful for diagnosing cloud properties (White et al. 1995, 1996). The Doppler acoustic sounder was added to the mix to provide high-resolution wind profiles in the lowest 200 m where the wind profiler has poor resolution and is affected by sea clutter. In this

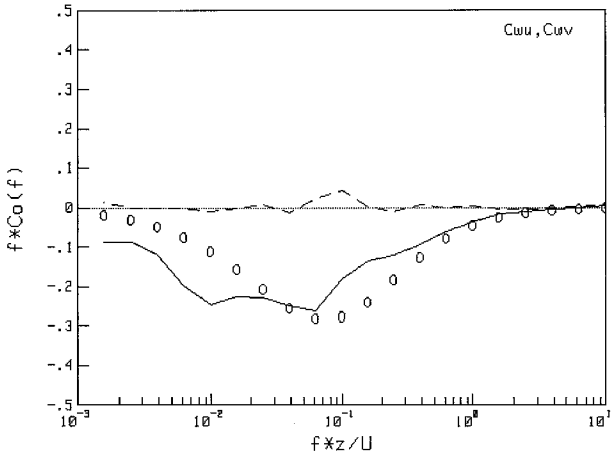

FIG. 5. Averages of *wu* (solid line) and *wv* (dashed line) near-neutral cospectra versus normalized frequency. The cospectra have been normalized by u^2(i.e., the area under the solid curve is -1.0). The circles are the neutral parameterization from Kaimal et al. (1972).

section, brief descriptions of these instruments will be provided.

a. Ceilometer

The lidar ceilometer is a commercially produced instrument designed for National Weather Service sites at airports. The wavelength is 0.904 μm with a pulse repetition rate between 620 and 1120 Hz. The unit has an internal processor that delivers backscatter-intensity profiles and computes cloud-base heights every 30 s. Special software written at The Pennsylvania State University for acquiring and displaying the cloud-base height and aerosol-backscatter intensity information is being used. The backscatter data gives an indication of cloud-base height even when a cloud is not directly overhead and also clearly define precipitation below the clouds. See Albrecht et al. (1990) or Chertock et al. (1993) for examples of use in the marine boundary layer.

b. Wind profiler/RASS

The wind profiler is a special seagoing version of the boundary-layer profiler developed at the NOAA Aeronomy Laboratory in Boulder, Colorado (Ecklund et al. 1988). Winds are obtained from the mean Doppler shift, and turbulence information can be deduced from the intensity and width of the Doppler spectrum (White and Fairall 1995). The system uses a flatplate, microstrip phased-array antenna with an aperture of 4 m^2. Three independent beam orientations are produced by electronically changing the phasing. A commercially available gyrostabilized platform (Seatel Inc.) is used to maintain the antenna level with respect to gravity, despite ship motion. After the antenna is installed on the pedestal, it is first statically balanced and then dynamically balanced. Electronic levels are installed on the

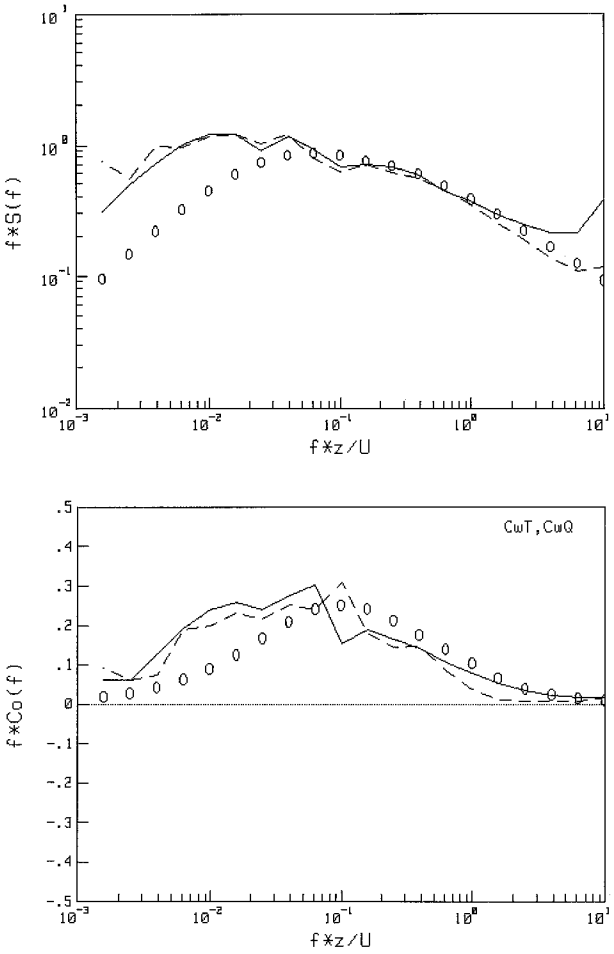

FIG. 6. Averaged scalar spectra and cospectra for near-neutral conditions: (a) the sonic temperature variance spectrum (solid line) and the IR-hygrometer humidity variance spectrum (dashed line) normalized as per Kaimal et al. (1972) and (b) the *wT* cospectrum (solid line) and the *wq* cospectrum (dashed line) normalized by $-u_*X_*$. In both graphs the circles are the Kaimal et al. (1972) near-neutral parameterization.

TABLE 3. ETL bulk meteorology and flux system measurement accuracies as estimated by Bradley et al. (1995).

Variable	Name	50-min rms	Mean bias
u (m s^{-1})	Wind speed	0.3	$\pm$0.2
T_a, day (K)	Air temp.	0.3	$\pm$0.2
T_a, night (K)	Air temp.	0.2	$\pm$0.1
q (g kg^{-1})	Humidity	0.3	$\pm$0.2
T_s (K)	Water temp.	0.1	$\pm$0.2
q_s (g kg^{-1})	Water sat. humidity	0.1	$\pm$0.2
H_s, cov (W m^{-2})	Sensible heat flux	3 $\pm$ 20%	$\pm$2
H_l, cov (W m^{-2})	Latent heat flux	5 $\pm$ 20%	$\pm$4
τ, cov (N m^{-2})	Stress	0.015 $\pm$ 30%	0.002
$\|\tau\|$, ID (N m^{-2})	Stress inertial	15%	0.002
R_s (W m^{-2})	Solar flux	1%	$\pm$4
R_l (W m^{-2})	IR flux	5	$\pm$2.5
Precip. (mm h^{-1})	Rain rate	15%	?

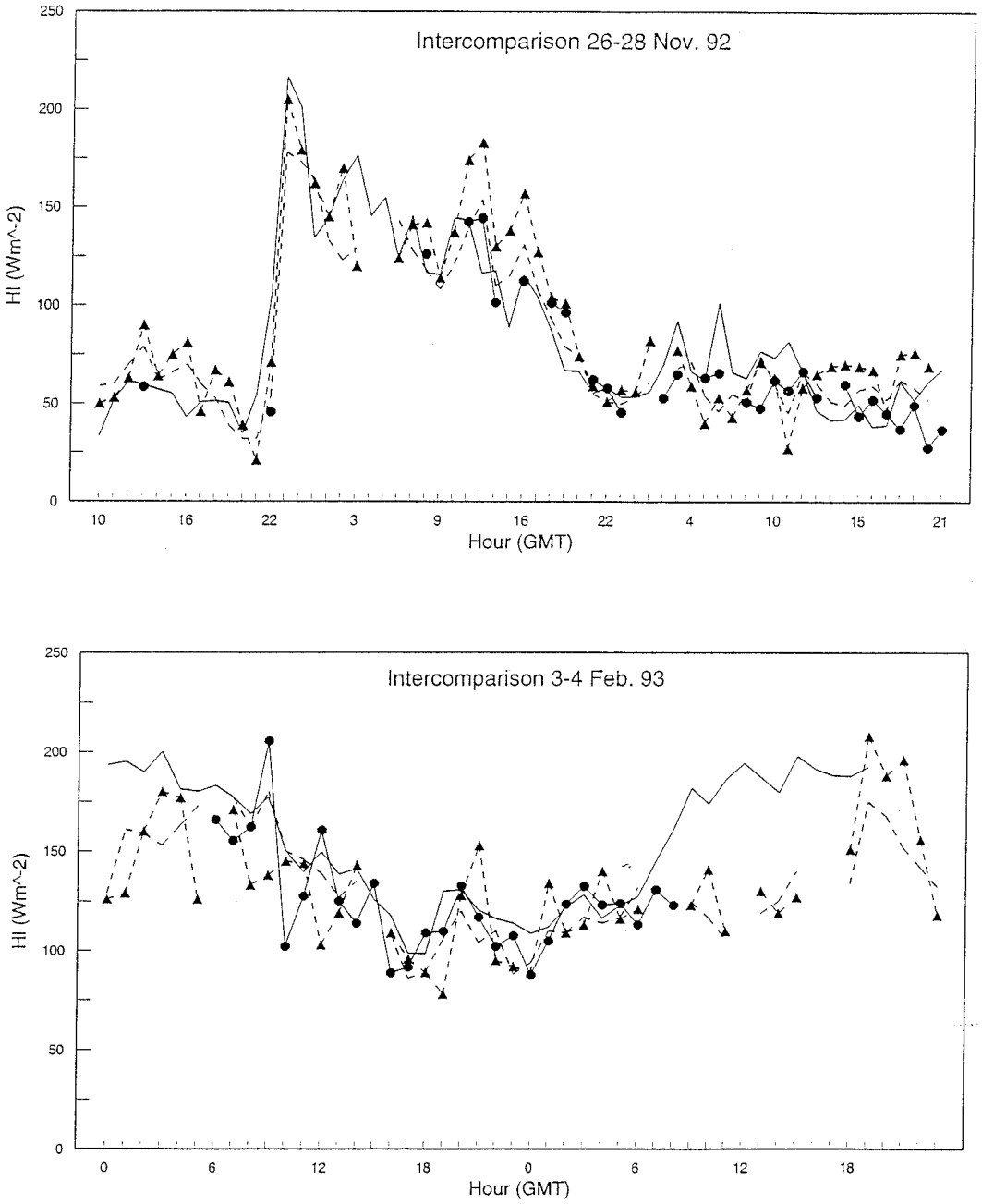

FIG. 7. Intercomparison of latent heat fluxes measured from the R/V *Franklin* (indicated as FR) and the R/V *Moana Wave* (indicated as MW) from two different periods during the TOGA COARE experiment. The dotted line represents the MW covariance values and the solid line the MW bulk estimate. The solid circles are the FR covariance values, and the dashed line is the FR bulk estimate. The ships are collocated only during the period when FR covariance values are given.

antenna for the balancing process and to monitor actual orientation at sea. Mean balance to within a fraction of a degree is obtained in port. Generally, the performance of the pedestal compensator is good, but on two cruises mean imbalance had to be corrected. Horizontal winds in fixed-earth coordinates are derived from the radial Doppler shifts with standard coordinate rotations (as in section 3a) using GPS data for ($\mathbf{V}_{lp}$) and the gyrocompass for heading. In the absence of precipitation, the vertical Doppler correction term is ignored. No attempt is made to correct for wave-induced errors. When the antenna is not level, the data clearly show erroneous changes in the wind vector as the ship maneuvers.

In the absence of precipitation, the radar-scattering

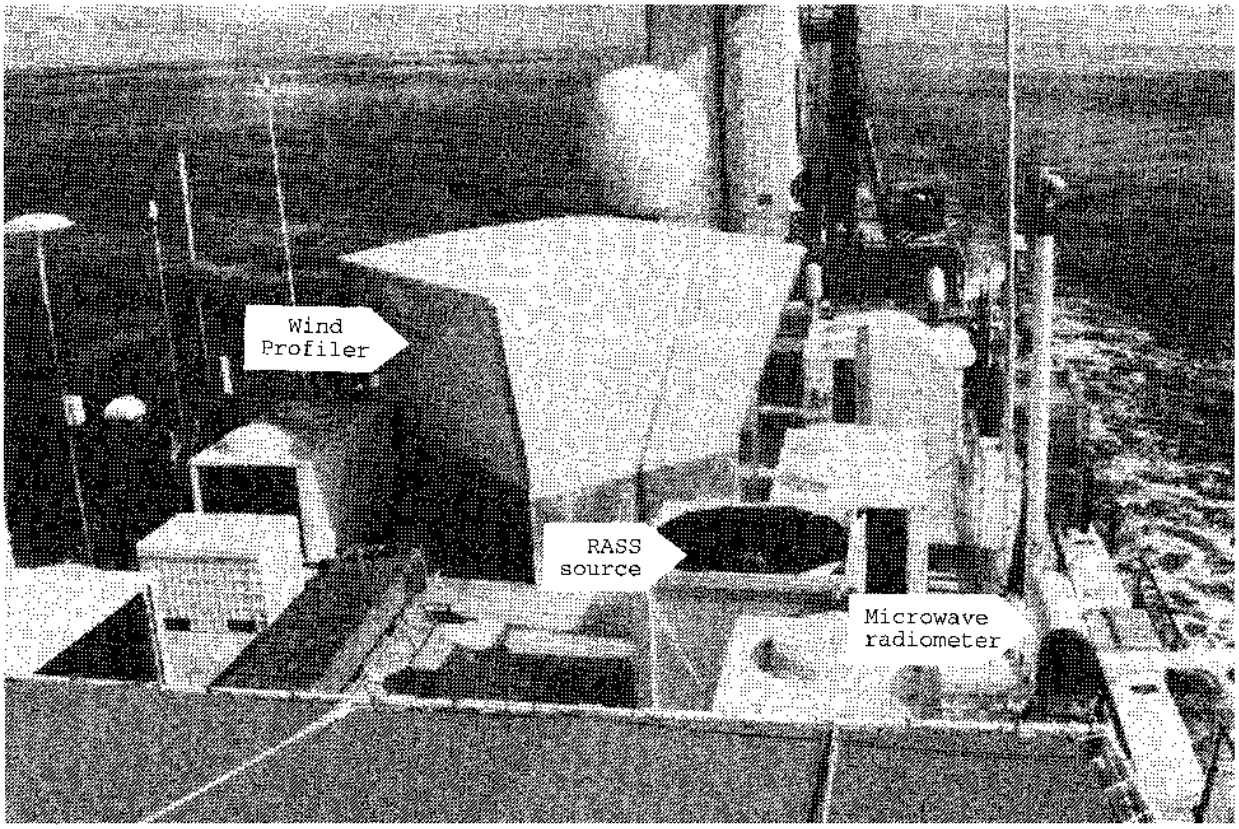

FIG. 8. Photograph of several remote sensors on the R/V *Moana Wave*.

originates from refractive-index inhomogeneities associated with atmospheric turbulence (see White et al. 1996 for a detailed discussion). In the Tropics, the maximum altitude of useful winds from the profiler is 2–3 km at 60-m vertical resolution and 3–5 km at 420-m vertical resolution. Real-time software is used to calculate the first three moments of the atmospheric scattering peak in the measured Doppler velocity spectrum. These moments are then used to compute profiles of the radar refractive-index structure function parameter C_n^2, the mean wind vector, and the rate of dissipation of turbulent kinetic energy ϵ (White and Fairall 1995). The top of the ABL is usually evident as a strong peak in C_n^2 or a rapid decrease with height of ϵ (White et al. 1991).

RASS capability is obtained by adding two acoustic sources to the radar and analyzing the velocity spectrum for Doppler shifts near the atmospheric speed of sound (about 340 m s^{-1}). Because the speed of sound is directly related to temperature, RASS is able to measure air temperature profiles, but at a range rarely exceeding 1 km with this unit. This poor performance compared to 405- and 50-MHz systems is caused by the small antenna size, low power, and strong acoustic absorption at 1.9 kHz. Best performance occurs for light winds or for moderate (5–10 m s^{-1}) winds with an acoustic source placed directly upwind of the radar antenna by a few tens of meters.

c. Microwave radiometer

The microwave radiometer is a small portable unit built by Radiometrics Corporation and modified for shipboard use by ETL. The radiometer provides continuous measurements of total integrated atmospheric water vapor and cloud liquid water content with a time resolution of about 30 s. On some cruises, a microwave radiometer designed and built at ETL has been used. Both systems typically use one channel in the 20-GHz water vapor absorption region and one channel in the 31-GHz liquid water absorption region. In some cases a third channel at 90 GHz is used to improve sensitivity to liquid water (Hogg et al. 1983). A retrieval method based on known or assumed profile statistics (e.g., from rawinsondes) is used to derive integrated water vapor and liquid (Hogg et al. 1983); accuracy for liquid water is estimated to be 20% (Fairall et al. 1990).

d. Rawinsonde

The rawinsonde system is an Omega version of the NCAR Cross-chain Loran Atmospheric Sounding Sys-

tem, designed for operation by one person. Navaid-based sondes (we use Vaisala RS-80-N) are particularly useful for wind finding from ships, where theodolite approaches are difficult to implement because of ship motion. Temperature, humidity, and pressure are obtained at roughly 50-m vertical resolution. Wind speed and direction are also calculated at 50-m intervals but are actually smoothed values computed from position readings from −300 m to +300 m.

e. Sodar

A Doppler minisodar from Aerovironment adds high-resolution detail to the wind profiles in the lowest 200 m. The radar wind profiler has 60-m range resolution and its first usable range gate at sea is often above 200 m. The sodar has a phased array antenna consisting of 49 acoustic drivers in a hexagonal pattern. The drivers are oriented horizontally and the beams are directed vertically off two reflecting surfaces. One vertical and two tilted beams are obtained by phasing the driving elements. The maximum vertical resolution for winds and backscatter intensity is 5 m. The acoustic frequency is tunable but is nominally set to 4.5 kHz. The system transmits a pulse about every 2 s, depending on maximum range selected. Time resolution for the backscatter intensity plots is nominally 10 s; for the average wind profiles it is 1–60 min. The antenna was mounted in a double-gimbaled cradle to compensate for ship motion. The gimbaling system was found to be underdamped in the first sea deployment (the MBL cruise off Monterey).

Tests of the sodar in Boulder indicated reliable wind profiles to maximum heights of 100–250 m depending on conditions. Performance at sea in the MBL cruise was much less impressive. This is believed to be partly due to the poor location of the instrument in a confined area on the ship. Thus, lower range gates were compromised by echoes from the ship's superstructure. Another factor is the much lower sensible heat flux typically found over the oceans (tens of watts per square meter) compared to over land (hundreds of watts per square meter). This device is primarily sensitive to C_T^2, which is directly related to the sensible heat flux through MOS scaling [see (2) and (7)]. A second sea trial was conducted in 1996.

5. Recent results

About 3500 nominally 1-h averages have been measured with the flux system since the first deployment in the COARE pilot cruise. An example from a single day with very steady conditions during the TIWE cruise is shown in Fig. 9. Bulk, inertial-dissipation, and covariance latent heat fluxes are all shown. The sensible heat fluxes are quite small, so only the covariance value is shown. Bulk, inertial-dissipation, and covariance friction velocity estimates show unusually good agreement, primarily due to steady conditions, a lack of precipitation, an absence of ship maneuvers, and fairly calm seas. Based on intercomparisons with buoys and other flux measuring platforms in the COARE experiment (E. Bradley et al. 1997, manuscript submitted to *J. Atmos. Oceanic Technol.*), we have estimated accuracies for these measurements as shown in Table 3. The system has been used in several investigations of flux parameterization. Young et al. (1992, 1995) examined the effects of deep convective structures on the surface energy budget of the equatorial Pacific. Ledvina et al. (1993) showed that bulk flux estimates are sensitive to the length of the average applied to the mean variables used in the algorithm. This was particularly critical for stress estimates where the use of daily averaged winds caused errors of a factor of 3. Fairall et al. (1996) used the measurements from the *Moana Wave* to develop a bulk algorithm that is being used by the entire COARE science community.

The past and future deployment of the system in many different marine regimes gives us the opportunity to develop a bulk parameterization that can be generally applied from the poles to the equator. An example is

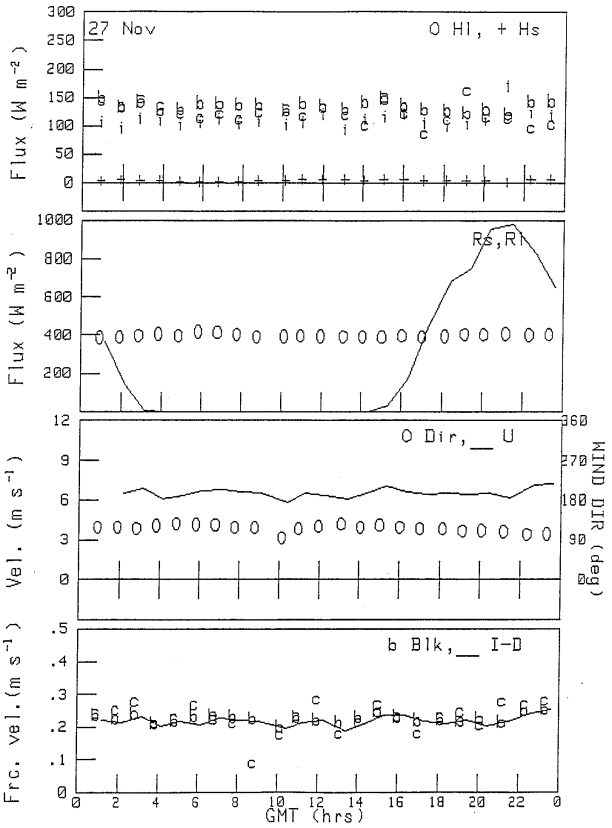

FIG. 9. Sample time series of fluxes and meteorology from TIWE. The upper panel shows the sensible heat flux (+) and three estimates (b—bulk, c—covariance, and i—inertial) of the latent heat flux. The second panel shows the solar (line) and IR (circle) radiative fluxes. The third panel shows the wind speed (line) and direction (circle). The lowest panel shows three estimates (b—bulk, c—covariance, and solid line—inertial) of friction velocity.

TABLE 4. Mean fluxes values from the SCOPE and COARE programs. The subscript *c* denotes covariance data and *b* denotes bulk estimates.

Variable	COARE	SCOPE
u (m s^{-1})	4.0	4.1
T_a (°C)	28.0	16.7
T_s (°C)	29.2	19.1
ΔT (°C)	1.2	2.4
q (g kg^{-1})	18.4	10.4
q_s (g kg^{-1})	24.8	13.4
Δq (g kg^{-1})	6.4	3.0
H_{sc} (W m^{-2})	8	17
H_{sb} (W m^{-2})	6	15
H_{lc} (W m^{-2})	95	50
H_{lb} (W m^{-2})	93	52
$\langle wu\rangle_c$ (m^2 s^{-2})	−0.022	−0.025
$\langle wu\rangle_b$ (m^2 s^{-2})	−0.024	−0.027
$\langle wv\rangle_c$ (m^2 s^{-2})	+0.003	−0.006
$\langle wv\rangle_b$ (m^2 s^{-2})	0	0
Number	860	180

given in Table 4, where average properties from deployments in the equatorial Pacific and the California coast are compared. Note that the mean wind speed for the two experiments is about the same, but the air–sea temperature difference is about a factor of 2 greater for California, and the air–sea humidity difference is about a factor of 2 greater for the Pacific. As expected from bulk concepts, the sensible and latent heat fluxes scale appropriately. Also note that the cross-stream stress (the *w*–*v* covariance) is small but not negligible, indicating that the mean stress vector is oriented about 10° from the mean wind vector. The sign of the cross-stream stress is consistent with the fact that COARE occurred at 2°S, but the physical significance is unknown.

The ceilometer is a very rugged and reliable instrument that has produced so much data that a single example does not do it justice. Instead, we offer a simple summary of cloud-base height and overhead cloud fraction statistics from deployment in four different climate regions (Table 5). More details can be found in White et al. (1995).

A time–height cross section of hourly average wind profiles from one day in the TIWE experiment is shown in Fig. 10. The height coverage is good in this example because the background humidity in the Tropics in much higher than what is often found in the midlatitudes. Note the inconsistent wind profile at about 1000 UTC. This is caused by a change of ship direction during the hour. At this date we were correcting winds with hourly average GPS and heading information. An example of RASS temperature performance from the SCOPE experiment in the region of San Clemente Island, off the coast of California, is shown in Fig. 11. An apparent isothermal layer appears near the surface in the contoured data because only one radar range gate is available in the lowest 200 m. In this case, the subsidence inversion is obvious as the region of tightly packed contours of RASS temperature (very close to virtual temperature) between 500 and 700 m. The base of the inversion inferred from radiosondes is indicated by the circled plus symbol. These data indicate a potential tem-

TABLE 5. Cloud statistics generated from extended time series of ceilometer data.

Experiment name	Dates	Location latitude (°) longitude (°)	Total number of 30-s profiles	Cloud fraction	Cloud base (m) 20th percentile	50th percentile	80th percentile	Primary cloud types
FIRE (First International Satellite Cloud Climatology Project Region Experiment)	Jul 1987	San Nicolas Island Eastern Pacific 33°N, 120°W						
		R/V *Titan*	8.05×10^4	0.69	300	457	750	Marine stratus
SCOPE (San Clemente Ocean Probing Experiment)	Sep 1993	Eastern Pacific 33°N, 118°W						
TIWE (Tropical Instability Wave Experiment)	Nov–Dec 1991	R/V *Moana Wave* Equatorial Pacific 0°, 140°W	5.68×10^4	0.26	625	945	1585	Trade cumulus
ASTEX (Atlantic Stratocumulus Transition Experiment)	Jun 1992	R/V *Malcom Baldridge* Eastern Atlantic 27°–37°N, 22°–27°W	5.81×10^4	0.45	594	1021	1463	Marine stratus trade cumulus
		Porto Santo Island 33°N, 16°W	3.07×10^4 (1-min profiles)	0.56	556	938	1494	Marine stratus trade cumulus
COARE (Coupled Ocean–Atmosphere Response Experiment)	Nov 1992–Feb 1993	R/V *Moana Wave* Western Pacific 2°S–5°N, 153°–157°E	1.26×10^5	0.22	686	1052	1844	Trade cumulus (suppressed) Cumulonimbus (convective)

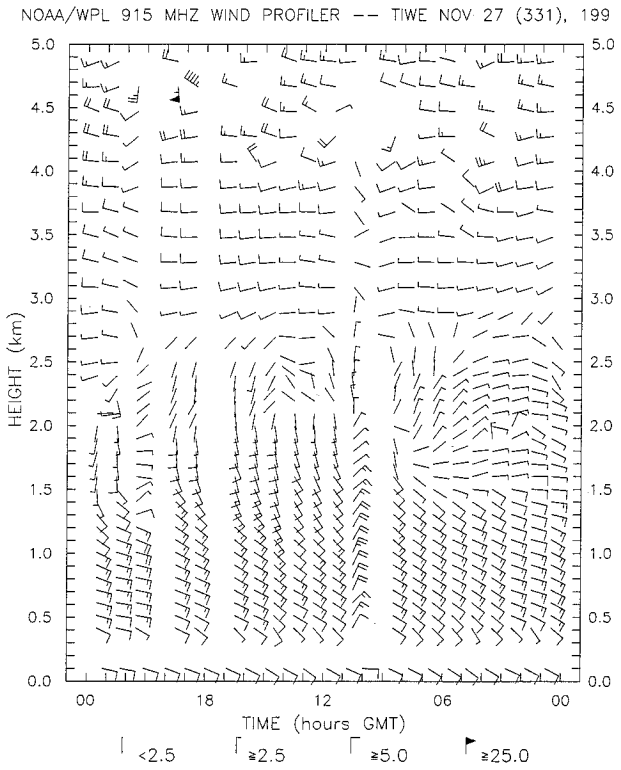

FIG. 10. Sample time–height wind barb plot from the 915-MHz wind profiler during TIWE. Note that time goes from right to left. The number of barbs indicates the wind speed (m s^{-1}), and the orientation designates the direction. The lowest wind barb is from the anemometer at 12-m height.

perature jump across the inversion of about 7 K with only a modest diurnal effect (local sunrise is at about 1400 UTC). On this day the winds were fairly weak, so conditions were favorable for good RASS height coverage. Typically, when the inversion height exceeds 1 km, identification by RASS becomes more erratic. RASS has about the same altitude coverage as sodar as both are adversely affected by advection of the acoustic beam by the horizontal wind. Sodar has superior vertical resolution, but unlike sodar, RASS can quantify the actual temperature change across the inversion.

An example of stratocumulus cloud information deduced from several remote sensors is displayed in Fig. 12. These data are from the ASTEX experiment near the Azore Islands. Cloud-base height and integrated liquid water content are directly obtained from the ceilometer and microwave radiometer. The cloud-top height is deduced from the sudden decrease in wind profiler backscatter intensity associated with the transition from the high moisture microturbulence intensity in the boundary layer to the relatively quiescent conditions above the inversion (Chertock et al. 1993). Note the strong correlation of cloud physical thickness with increased liquid water content; for very thin clouds the liquid water content is at the sensitivity threshold of the radiometer. The values here often indicate a subadiabatic liquid water cloud structure suggesting weak turbulent mixing. Note the existence of cumulus clouds beneath the upper stratus layer as indicated by lower cloud bases and increased liquid water amounts. The peak in liquid water content near 1730 UTC corresponds to drizzle that did not quite reach the surface.

In Fig. 13 we highlight the turbulence measuring ca-

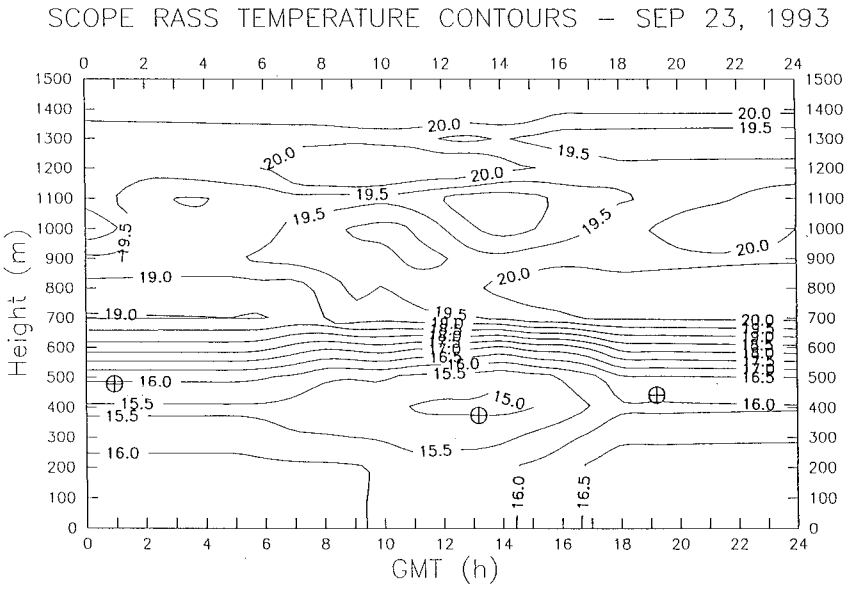

FIG. 11. Sample time–height cross section of RASS-derived sonic temperature from 23 September 1993, during the SCOPE experiment off southern California. The circled plus symbols denote inversion base heights deduced from radiosonde temperature and humidity profiles.

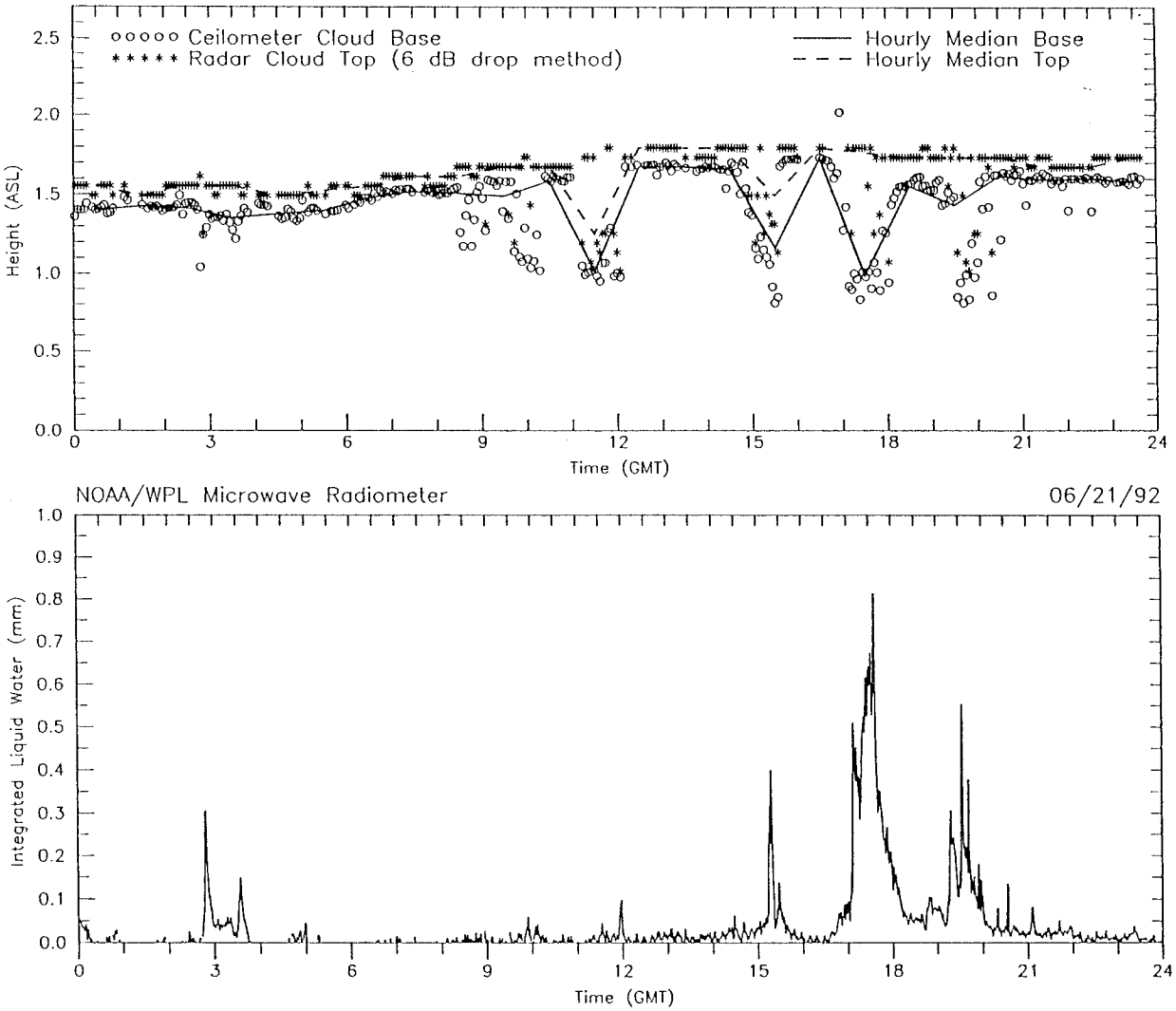

FIG. 12. Sample time series of stratocumulus cloud properties from ASTEX. The upper panel shows the profiler-deduced values for cloud-top height (asterisk and dashed line) and the ceilometer values for cloud-base height (circle and solid line). The lower panel shows the microwave radiometer values for integrated cloud liquid water content.

pabilities of these remote sensors for the same period shown in Fig. 12. Here the upper panel shows the vertical velocity, the middle panel C_n^2, and the lower panel C_u^2 (proportional to $\epsilon^{2/3}$). The data shown are for 30-s samples taken every 3 min with 60-m height resolution in the vertical beam. In the upper panel the mottled regions of random red and dark blue dots indicate background noise (i.e., invalid data). These regions are apparent above 1.7 km in the first part of the record and in various intervals between 0.6 and 1.7 km; they correlate with regions of low signal (blue colors) in the second panel and represent C_n^2 values below the sensitivity threshold of the profiler. Note the very thin region between 1.7 and 2.0 km of enhanced C_n^2 in the middle panel and valid vertical velocities in the upper panel, both associated with the trade-wind inversion. The drizzle that occurred at 1730 UTC is apparent in the blue region of negative vertical velocity (about 1 m s^{-1}) in the upper panel. The lower panel shows a strong region of velocity turbulence near the surface associated with surface shear generation of turbulent kinetic energy. There is also a hint of turbulence enhancement at the inversion, indicating some modest mean velocity shear in that region. The apparent increase of C_u^2 during the drizzle event is an artifact due to Doppler width broadening by the range of fall velocities existing in the precipitation (i.e., a spectrum of drizzle droplets). Also note the strong patches of C_n^2 and somewhat weaker response of C_u^2 associated with patchy cumulus clouds in the middle of the boundary layer, indicated by the groups of black dots denoting ceilometer measurements of fractal cumulus below the stratus layer.

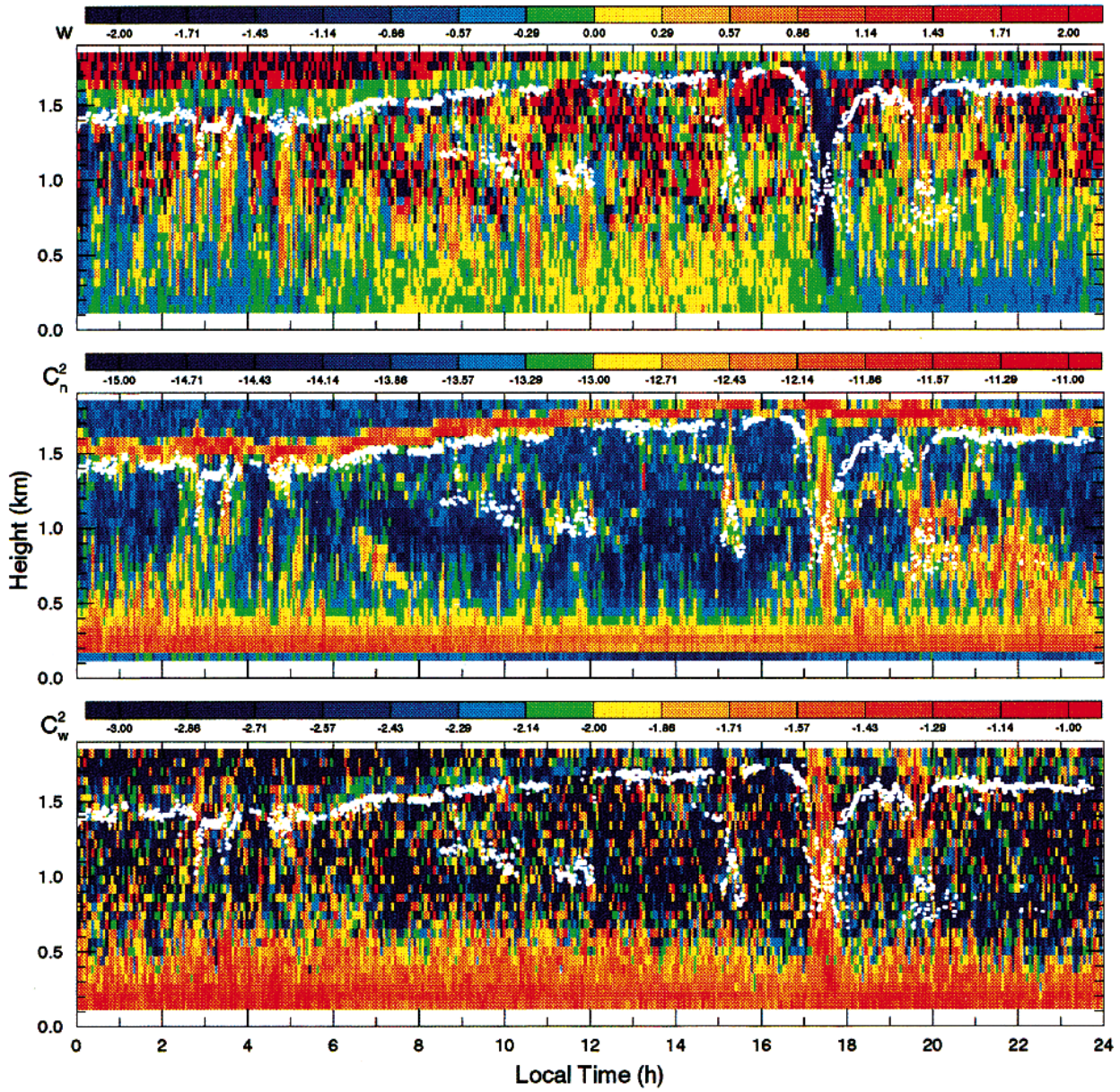

FIG. 13. Turbulence profile time series corresponding to Fig. 12. The upper panel shows vertical velocity, the middle panel C_n^2, and the lower panel C_w^2. The color coding is described by the color bar above each panel. The total height range is from 0.15 to 2.0 km in 60-m range gates; the time resolution is a 30-s sample every 3 min. The black dots on the middle panel are cloud-base heights from the ceilometer.

6. Discussion

After five years of steady development, a seagoing system capable of complete surface flux and sophisticated boundary layer profile measurements has been demonstrated. The system has application in a variety of research areas in marine meteorology, including oceanic surface energy budgets, boundary layer dynamics, dispersion/diffusion, air–sea gas and particle transfer, entrainment, and cloud–radiation coupling. So far, the system has been used for research in the areas of surface flux parameterization (Fairall et al. 1996), flux averaging issues (Ledvina et al. 1993), the atmospheric turbulent kinetic energy budget (Fairall and Edson 1994), precipitation contributions to surface heat flux (Gosnell et al. 1995), cloud-radiative properties (Chertock et al. 1993; White et al. 1995), the coupling of surface fluxes and deep convection (Young et al. 1992, 1995), oceanic near-surface dynamics (Webster et al. 1996), and development of satellite algorithms (Clayson et al. 1996). Some of this research does not make use of the multiparameter nature of these data, but much of it does. Table 6 summarizes the unique collection of datasets

TABLE 6. Campaign hourly data statistics.

Variable	ASTEX			TIWE
	Median	Average	Sigma	Average
Ship speed (m s^{-1})	6.0	4.8	2.58	0.7
10-m wind speed (m s^{-1})	4.7	4.4	1.79	6.4
10-m wind direction (°)	33	34	77	108
Sea surface temperature (°C)	20.7	20.7	1.05	72.2
14-m air temperature (°C)	20.0	19.8	1.10	26.9
Surface saturation humidity (g kg^{-1})	15.2	15.2	0.97	22.5
14-m humidity (g kg^{-1})	10.5	10.5	1.35	17.1
14-m relative humidity (%)	73.2	72.8	7.71	77.3
Sensible heat flux (W m^{-2})	8	8	5.75	4
Latent heat flux (W m^{-2})	75	76	32.2	101
Surface stress (N m^{-2})	0.023	0.029	0.020	0.054
Surface solar irradiance R_s (W m^{-2})	58	255	320	232
Surface longwave irradiance (W m^{-2})	346	350	21.8	401
Total surface energy (W m^{-2})	−98	83	305	52
Transmission coefficient Tr	0.73	0.72	0.21	0.74
Albedo Re	0.26	0.27	0.20	0.22
Cloud optical depth τ_c	4.9	10.1	21.9	17.7
Cloud fraction at zenith f	0.26	0.38	0.37	0.26
Cloud base (m)	869	1007	515	886
Cloud thickness (m)	220	251	163	313
Cloud liquid water path* LWP (g m^{-2})		123		209

* From ASTEX, the average cloud LWP is defined as the average LWP measured by the radiometer divided by the average cloud fraction measured at zenith.

from two different marine climate regions. The data include surface mean meteorology, fluxes, and a variety of cloud characteristics including mean cloud fraction, height, physical thickness, optical thickness, and integrated liquid water content. Such comprehensive, synergistic, and high-quality data have never been available before and are potentially quite useful for climate analysts and modelers. Improvements in sensors, techniques, and experience will lead to increased use and integration of the data.

A second-generation flux system has been developed. This system has true real-time motion corrections and will be used for future work in gas flux research. Both eddy correlation and relaxed eddy accumulation techniques are planned. Plans to truly integrate the measurement systems by ethernet link are also being developed. A cruise conducted in the equatorial Pacific during March 1996 saw the addition of the Los Alamos National Laboratory UV-Raman lidar and the University of Massachusetts 35-GHz and 95-GHz cloud profiling radars. An ''unattended'' lidar and cloud radar are being developed at ETL for future deployments. These systems greatly increase the cloud and ABL measurement capabilities. Cloud radars have the ability to provide profiles of liquid water and cloud droplet size within clouds; drizzle droplet size and number concentration can also be profiled (Frisch et al. 1995). A Doppler lidar can measure subcloud ABL structures and turbulence profiles. This array of sensors represents the most comprehensive investigations of the marine ABL yet attempted. Combining with aircraft and/or satellite measurements will further increase observing capabilities and the potential for useful research.

Acknowledgments. The authors wish to acknowledge early contributions and inspirations from Profs. Dennis Thomson and Bruce Albrecht of The Pennsylvania State University. Thanks to Warner Ecklund and Ken Gage of the NOAA Aeronomy Laboratory and to Walt Dabberdt, Hal Cole, and Ned Chamberlain of the National Center for Atmospheric Research for close cooperation in producing the seagoing versions of the wind profiler and the sonde system. The engineering, technical, and scientific contributions of Dave Gregg, Scott Abbott, Jesse Leach, Cat Russell, and Norbert Szczepczynski are also acknowledged. Critical reviews by M. J. Post and one anonymous reviewer helped improve the manuscript. Partial support for this research has been provided by the Department of Energy Atmospheric Radiation Measurement program, the Office of Naval Research Marine Meteorology Program, the U.S. National Oceanic and Atmospheric Administration (NOAA) Climate and Global Change Program, and the joint NOAA/Department of Defense Advanced Sensor Applications Program.

REFERENCES

Alados-Arboledas, L., J. Vida, and J. I. Jimenez, 1988: Effects of solar radiation on the performance of pyrgeometers with silicon domes. *J. Atmos. Oceanic Technol.,* **5,** 666–670.

Albrecht, B. A., and S. K. Cox, 1977: Procedures for improving pyrgeometer performance. *J. Appl. Meteor.,* **16,** 188–197.

——, C. W. Fairall, D. W. Thomson, A. B. White, and J. B. Snider, 1990: Surface-based remote sensing of the observed and the adiabatic liquid water content of stratocumulus clouds. *Geophys. Res. Lett.,* **17,** 89–92.

Axford, D. N., 1968: On the accuracy of wind measurements using an inertial platform in an aircraft and an example of a mea-

surement of the vertical mesostructure of the atmosphere. *J. Appl. Meteor.,* **7,** 645–666.
Blanc, T. V., 1985: Variation of bulk-derived surface flux, stability, and roughness results due to the use of different transfer coefficient schemes. *J. Phys. Oceanogr.,* **15,** 650–669.
——, 1986: The effect of inaccuracies in weather-ship data on bulk-derived estimates of flux, stability, and sea-surface roughness. *J. Atmos. Oceanic Technol.,* **3,** 12–26.
——, 1987: Accuracy of bulk-method-determined flux, stability, and sea surface roughness. *J. Geophys. Res.,* **92,** 3867–3876.
Brost, R. A., J. C. Wyngaard, and D. H. Lenschow, 1982: Marine stratocumulus layers. Part II: Turbulence budgets. *J. Atmos. Sci.,* **39,** 818–831.
Browning, K. A., 1994: Survey of perceived priority issues in the parameterizations of cloud-related processes in GCMs. *Quart. J. Roy. Meteor. Soc.,* **120,** 483–487.
Brutsaert, W., 1982: *Evaporation into the Atmosphere.* D. Reidel, 299 pp.
Businger, J. A., 1986: Evaluation of the accuracy with which dry deposition can be measured with current micrometeorological techniques. *J. Climate Appl. Meteor.,* **25,** 1100–1123.
——, and S. P. Oncley, 1990: Flux measurements with conditional sampling. *J. Atmos. Oceanic Technol.,* **7,** 349–352.
Cerni, T. A., D. A. Hanschulz, L. D. Nelson, and D. Rottner, 1987: An atmospheric infrared hygrometer. Preprints, *Proc. Sixth Symp. on Meteorological Observations and Instrumentation,* New Orleans, LA, Amer. Meteor. Soc., 205–208.
Charnock, H., 1955: Wind stress on a water surface. *Quart. J. Roy. Meteor. Soc.,* **81,** 639.
Chertock, B., C. W. Fairall, and A. B. White, 1993: Surface-based measurements and satellite retrievals of broken cloud properties in the equatorial Pacific. *J. Geophys. Res.,* **98,** 18 489–18 500.
Clayson, C. A., J. A. Curry, and C. W. Fairall, 1996: Evaluation of turbulent fluxes at the ocean surface using surface renewal theory. *J. Geophys. Res.,* **101,** 28 503–28 513.
Deardorff, J. W., 1974: Three-dimensional numerical study of turbulence in an entraining mixed layer. *Bound.-Layer Meteor.,* **7,** 199–226.
Donelan, M. A., 1990: Air–sea interactions. *The Sea: Ocean Engineering Science,* Vol. 9, E. D. Goldberg and Coeditors, Wiley-Interscience, 239–292.
Ecklund, W. L., D. A. Carter, and B. B. Balsley, 1988: A UHF profiler for the boundary layer: Brief description and initial results. *J. Atmos. Oceanic Technol.,* **5,** 432–441.
Edson, J. B., C. W. Fairall, P. G. Mestayer, and S. E. Larsen, 1991: A study of the inertial-dissipation method for computing air–sea fluxes. *J. Geophys. Res.,* **96,** 10 689–10 711.
Fairall, C. W., 1984: Interpretation of eddy-correlation measurements of particulate deposition and aerosol flux. *Atmos. Environ.,* **18,** 1329–1337.
——, 1987: Similarity theories and microturbulence in the atmospheric mixed layer. *Dynamics of the Oceanic Mixed Layer, Proceedings of the Fourth Hawaiian Winter Workshop,* P. Muller and D. Henderson, Eds., Hawaiian Institute of Geophysics Special Publications, 265–291.
——, and S. E. Larsen, 1986: Inertial-dissipation methods and turbulent fluxes at the air–ocean interface. *Bound.-Layer Meteor.,* **34,** 287–301.
——, and R. A. Markson, 1987: Mesoscale variations in surface stress, heat fluxes, and drag coefficient in the marginal ice zone during the 1983 Marginal Ice Zone Experiment. *J. Geophys. Res.,* **92,** 6921–6932.
——, and G. S. Young, 1991: A field evaluation of shipboard performance of an infrared hygrometer. Preprints, *Seventh Symp. on Meteorological Observations and Instrumentation,* New Orleans, LA, Amer. Meteor. Soc., 311–315.
——, and M. McPhaden, 1993: A ship-buoy comparison of bulk meteorological measurements and implications for surface flux estimates. *Extended Abstracts, Third Scientific Meeting of the Oceanography Society,* Seattle, WA, Oceanogr. Soc., 51–52.
——, and J. B. Edson, 1994: Recent measurements of the dimensionless turbulent kinetic energy dissipation function over the ocean. Preprints, *Second Int. Conf. on Air–Sea Interaction and Meteorology and Oceanography of the Coastal Zone,* Lisbon, Portugal, Amer. Meteor. Soc., 224–225.
——, ——, S. E. Larsen, and P. G. Mestayer, 1990: Inertial-dissipation air–sea flux measurements: A prototype system using real-time spectral computations. *J. Atmos. Oceanic Technol.,* **7,** 425–453.
——, E. F. Bradley, D. P. Rogers, J. B. Edson, and G. S. Young, 1996: Bulk parameterization of air–sea fluxes for Tropical Ocean–Global Atmospheric Coupled Ocean–Atmosphere Response Experiment. *J. Geophys. Res.,* **101,** 3747–3764.
Frisch, A. S., C. W. Fairall, and J. B. Snider, 1995: On the measurement of stratus cloud and drizzle parameters with a K_α-band Doppler radar and a microwave radiometer. *J. Atmos. Sci.,* **52,** 2788–2799.
Fujitani, T., 1985: Method of turbulent flux measurement on a ship by using a stable platform system. *J. Meteor. Soc. Japan,* **36,** 157–170.
Garratt, J. R., 1992: *The Atmospheric Boundary Layer.* Cambridge University Press, 316 pp.
Gautier, C., G. Diak, and S. Masse, 1980: A simple physical model to estimate incident solar radiation at the surface from GEOS satellite data. *J. Appl. Meteor.,* **19,** 1005–1012.
Geernaert, G. L., 1990: Bulk parameterizations for the wind stress and heat fluxes. *Surface Waves and Fluxes,* Vol. I, G. L. Geernaert and W. J. Plant, Eds., Kluwer, 91–172.
Godfrey, J. S., and A. C. M. Beljaars, 1991: On the turbulent fluxes of buoyancy, heat, and moisture at the air–sea interface at low wind speeds. *J. Geophys. Res.,* **96,** 22 043–22 048.
Gosnell, R., C. W. Fairall, and P. J. Webster, 1995: The surface sensible heat flux due to rain in the tropical Pacific Ocean. *J. Geophys. Res.,* **100,** 18 437–18 442.
Hare, J. E., J. B. Edson, and C. W. Fairall, 1992: Progress on real-time covariance measurements of air–sea fluxes from ships and buoys. Preprints, *10th Symp. on Turbulence and Diffusion,* Portland, OR, Amer. Meteor. Soc., 281–284.
Hasse, L., 1971: The sea surface temperature deviation and heat flow at the air–sea interface. *Bound.-Layer Meteor.,* **1,** 368–379.
Hogg, D. C., F. O. Guiraud, J. B. Snider, M. T. Decker, and E. R. Westwater, 1983: A steerable dual-channnel microwave radiometer for measurement of water vapor and liquid in the atmosphere. *J. Climate Appl. Meteor.,* **22,** 789–806.
Kaimal, J. C., J. C. Wyngaard, Y. Izumi, and O. R. Cote, 1972: Spectral characteristics of surface layer turbulence. *Quart. J. Roy. Meteor. Soc.,* **98,** 563–589.
——, ——, D. A. Haugen, O. R. Cote, Y. Izumi, S. J. Caughey, and C. J. Readings, 1976: Turbulence structure in the convective boundary layer. *J. Atmos. Sci.,* **33,** 2152–2169.
——, S. F. Clifford, and R. J. Laitaitis, 1989: Effect of finite sampling on atmospheric spectra. *Bound.-Layer Meteor.,* **47,** 337–347.
Katsaros, K. B., 1990: Parameterization schemes and models for estimating the surface radiation budget. *Surface Waves and Fluxes,* Vol. II, G. L. Geernaert and W. J. Plant, Eds., Kluwer, 91–172.
——, and J. E. DeVault, 1986: On irradiance measurement errors at sea due to tilt of pyranometers. *J. Atmos. Oceanic Technol.,* **3,** 740–745.
Kraus, E. B., and J. A. Businger, 1994: *Atmosphere–Ocean Interaction.* Oxford University Press, 352 pp.
Kristensen, L. K., J. Mann, and S. P. Oncley, 1997: How close is close enough when measuring scalar fluxes with displaced sensors? *J. Atmos. Oceanic Technol.,* in press.
Large, W. G., and S. Pond, 1981: Open ocean momentum flux measurements in moderate to strong winds. *J. Phys. Oceanogr.,* **11,** 324–336.
——, and ——, 1982: Sensible and latent heat flux measurements over the ocean. *J. Phys. Oceanogr.,* **12,** 464–482.
Larsen, S. E., J. B. Edson, C. W. Fairall, and P. G. Mestayer, 1993:

Measurement of temperature spectra by a sonic anemometer. *J. Atmos. Oceanic Technol.,* **10,** 345–354.

Ledvina, D. V., G. S. Young, R. A. Miller, and C. W. Fairall, 1993: The effect of averaging on bulk estimates of heat and momentum fluxes for the tropical western Pacific Ocean. *J. Geophys. Res.*, **98,** 20 211–20 217.

Lenschow, D. H., 1973: Two examples of planetary boundary layer modification over the Great Lakes. *J. Atmos. Sci.,* **30,** 568–581.

——, 1986: *Probing the Atmospheric Boundary Layer*. Amer. Meteor. Soc., 269 pp.

——, and L. K. Kristensen, 1985: Uncorrelated noise in turbulence measurements. *J. Atmos. Oceanic Technol.,* **2,** 68–81.

——, and P. Spyers-Duran, 1987: Measurements techniques: Air motion sensing. NCAR Bulletin 23, 361 pp. [Available from National Center for Atmospheric Research, P.O. Box 3000, Boulder, CO 80303.]

Liu, W. T., 1990: Remote sensing of surface turbulence heat flux. *Surface Waves and Fluxes*, Vol. II, G. L. Geernaert and W. J. Plant, Eds., Kluwer, 293–310.

——, K. B. Katsaros, and J. A. Businger, 1979: Bulk parameterization of the air–sea exchange of heat and water vapor including the molecular constraints at the interface. *J. Atmos. Sci.,* **36,** 1722–1735.

MacWhorter, M. A., and R. A. Weller, 1991: Error in measurements of incoming solar radiation made from ships and buoys. *J. Atmos. Oceanic Technol.,* **8,** 108–117.

Mahrt, L., D. Vickers, J. Howell, J. Hojstrup, M. Courtney, J. M. Wilczak, J. B. Edson, and J. Hare, 1996: Surface drag coefficients in RASEX. *J. Geophys. Res.,* **101,** 14 327–14 335.

Moeng, C.-H., 1984: A large-eddy simulation model for the study of planetary boundary-layer turbulence. *J. Atmos. Sci.,* **41,** 2052–2062.

——, S. Shen, and D. A. Randall, 1992: Physical processes with the nocturnal stratus-topped boundary layer. *J. Atmos. Sci.,* **49,** 2384–2401.

Mortensen, N. G., 1994: Flow response characteristics of the Kaijo Denki omni-directional sonic anemometer. Riso National Laboratory Rep. Riso-R-704(EN), 31 pp.

Nichols, S., 1984: The dynamics of stratocumulus: Aircraft observations and comparisons with a mixed layer model. *Quart. J. Roy. Meteor. Soc.*, **110,** 783–820.

Oncley, S. P., 1989: Flux parameterization techniques in the atmospheric surface layer. Ph.D. dissertation, University of California, Irvine, 202 pp. [Available from Dept. Mechanical Engineering, University of California, Irvine, Irvine, CA 92716.]

Oost, W. A., C. W. Fairall, J. B. Edson, S. D. Smith, R. J. Anderson, J. A. B. Wills, K. B. Katsaros, and J. DeCosmo, 1994: Flow distortion calculations and their application in HEXMAX. *J. Atmos. Oceanic Technol.,* **11,** 366–386.

Panofsky, H. A., and J. A. Dutton, 1984: *Atmospheric Turbulence.* Wiley-Interscience, 397 pp.

Pattey, E., R. L. Desjardins, and P. Rochette, 1993: Accuracy of the relaxed eddy-accumulation technique, evaluated using CO_2 flux measurements. *Bound.-Layer Meteor.*, **66,** 341–355.

Paulson, C. A., 1970: The mathematical representation of windspeed and temperature profiles in the unstable atmospheric surface layer. *J. Appl. Meteor.,* **9,** 857–861.

——, and J. J. Simpson, 1981: The temperature difference across the cool skin of the ocean. *J. Geophys. Res.,* **86,** 11 044–11 504.

Ruffieux, D., P. O. G. Persson, C. W. Fairall, and D. E. Wolfe, 1995: Ice pack and lead surface energy budgets during LEADEX 1992. *J. Geophys. Res.,* **100,** 4593–4612.

Saunders, P. M., 1967: The temperature at the ocean–air interface. *J. Atmos. Sci.,* **24,** 269–273.

Schmitt, K. F., C. A. Friehe, and C. H. Gibson, 1978: Humidity sensitivity of atmospheric temperature sensors by salt contamination. *J. Phys. Oceanogr.,* **8,** 141–161.

Schotanus, P., F. T. M. Nieuwstadt, and R. A. R. deBruin, 1983: Temperature measurement with a sonic anemometer and its application to heat and moisture fluxes. *Bound.-Layer Meteor.,* **26,** 81–93.

Skupniewicz, C. E., and K. L. Davidson, 1991: Hot-film measurements from a small buoy: Surface wind stress estimates using the inertial dissipation method. *J. Atmos. Oceanic Technol.,* **8,** 309–321.

Smith, S. D., 1988: Coefficients for sea surface wind stress, heat flux, and wind profiles as a function of wind speed and temperature. *J. Geophys. Res.,* **93,** 15 467–15 472.

Stage, S. A., and J. A. Businger, 1980: A model for entrainment into a cloud-topped marine boundary layer. Part II: Discussion of model behavior and comparison with other cloud models. *J. Atmos. Sci.*, **38,** 2230–2242.

Tanner, C. B., and G. W. Thurtell, 1969: Anemoclinometer measurements of Reynolds stress and heat transport in the atmospheric surface layer. University of Wisconsin Tech. Rep. ECOM-66-G22-F, 82 pp. [Available from US Army Electronic Command, Atmospheric Sciences Laboratory, Ft. Huachuca, AZ 85613.]

Vogel, C. A., and P. Frenzen, 1992: A new study of the TKE budget in the surface layer. Part II: The dissipation function and divergent transport terms. Preprints, *10th Symp. on Turbulence and Diffusion*, Portland, OR, Amer. Meteor. Soc., 161–164.

Webster, P. J., C. A. Clayson, and J. A. Curry, 1996: Clouds, radiation, and the diurnal cycle of sea surface temperature in the tropical western Pacific. *J. Climate,* **9,** 1712–1730.

White, A. B., and C. W. Fairall, 1995: Wind profiler measurements of scalar and velocity microturbulence profiles in the convective atmospheric boundary layer. Preprints, *11th Symp. on Boundary Layers and Turbulence*, Charlotte, NC, Amer. Meteor. Soc., 548–551.

——, ——, and D. W. Thomson, 1991: Radar observations of humidity variability in and above the marine atmospheric boundary layer. *J. Atmos. Oceanic Technol.,* **8,** 639–658.

——, ——, and J. B. Snider, 1995: Surface-based remote sensing of marine boundary-layer cloud properties. *J. Atmos. Sci.,* **52,** 2827–2838.

——, ——, A. S. Frisch, B. W. Orr, and J. B. Snider, 1996: Recent radar measurements of turbulence and microphysical parameters in clouds. *Atmos. Res.,* **40,** 177–221.

Wick, G. A., W. J. Emery, L. H. Kantha, and P. Schluessel, 1996: The behavior of the bulk-skin sea surface temperature difference under varying wind speed and heat flux. *J. Phys. Oceanogr.,* **26,** 1969–1988.

Willis, G. E., and J. W. Deardorff, 1974: A laboratory model of the unstable planetary boundary layer. *J. Atmos. Sci.,* **31,** 1297–1307.

Wyngaard, J. C., 1973: On surface-layer turbulence. *Workshop on Micrometeorology*, D. A. Haugen, Ed., Amer. Meteor. Soc., 101–149.

——, I. Izumi, and S. A. Collins, 1971: Behavior of the refractive index structure parameter near the ground. *J. Opt. Soc. Amer.,* **61,** 1646–1650.

Yelland, M. J., P. K. Taylor, I. E. Consterdine, and M. H. Smith, 1994: The use of the inertial dissipation technique for shipboard wind stress determination. *J. Atmos. Oceanic Technol.,* **11,** 1093–1108.

Young, G. S., D. R. Ledvina, and C. W. Fairall, 1992: Influence of precipitating convection on the surface energy budget observed during a Tropical Ocean Global Atmosphere pilot cruise in the tropical western Pacific Ocean. *J. Geophys. Res.*, **97,** 9595–9603.

——, S. M. Perugini, and C. W. Fairall, 1995: Convective wakes in the equatorial Pacific during TOGA COARE. *Mon. Wea. Rev.,* **123,** 110–123.